Evaluation of six geothermal heat flux maps for the Antarctic Lambert-Amery glacial system

Haoran Kang[1], Liyun Zhao[1,~~2~~*], Michael ~~Wolovick[1,5]~~Wolovick[4], John C. Moore[1,~~2,~~3,4*]

[1] College of Global Change and Earth System Science, Beijing Normal University, Beijing 100875, China

~~[2] Southern Marine Science and Engineering Guangdong Laboratory (Zhuhai), China~~

[~~3~~2] CAS Center for Excellence in Tibetan Plateau Earth Sciences, Beijing 100101, China

[~~4~~3] Arctic Centre, University of Lapland, Rovaniemi, Finland

[~~5~~4] Alfred Wegener Institute, Bremerhaven, Germany

* Corresponding author

Corresponding author: Liyun Zhao (zhaoliyun@bnu.edu.cn); John C. Moore (john.moore.bnu@gmail.com)

Abstract

Basal thermal conditions play an important role in ice sheet dynamics, and they are sensitive to geothermal heat flux (GHF). Here we estimate the basal thermal conditions, including basal temperature, basal melt rate, and friction heat underneath the Lambert-Amery glacier system in east Antarctica, using a combination of a forward model and an inversion from a 3D ice flow model. We assess the sensitivity and uncertainty of basal thermal conditions using six different GHFs. We evaluate the modelled results using all ~~available~~ observed subglacial lakes. ~~There are very~~The different GHFs lead to large differences in ~~modelled~~simulated spatial ~~pattern~~patterns of temperate basal conditions ~~using the different GHFs.~~. The two ~~most~~ recent GHF fields inverted from aerial geomagnetic observations have ~~higher values of~~the highest GHF ~~in the region~~, produce ~~a larger~~the largest warm-based area, and match the observed distribution of subglacial lakes better than the other GHFs. ~~The fast flowing glacier region has a lower modelled basal friction coefficient, faster basal velocity, with higher basal frictional heating in the range of 50-2000 mW m^{-2} than the base under slower flowing glaciated areas.~~ The modelled basal melt rate reaches ten to hundreds of mm per year locally in Lambert, Lepekhin and Kronshtadtskiy glaciers feeding the Amery ice shelf, and ranges from 0-5 mm yr^{-1} on the temperate base of the vast inland region.

1 Introduction

The Lambert-Amery system in East Antarctica is believed to be relatively stable against climate change and has changed little over several decades of observations (King et al., 2007). However, there is also evidence of extensive subglacial rifts and lakes~~.~~ (Fretwell et al., 2013; Jamieson et al~~.~~., 2016; Cui et al., 2020a). Jamieson et al. (2016) report a large subglacial drainage network~~, suggesting that~~ in Princess Elizabeth Land (PEL), which would transport water from central PEL toward the Lambert-Amery region ~~could respond rapidly to changes in~~ . The complexity of the subglacial environment may influence the stability and basal ~~water supply or, potentially to surface forcing~~mass balance of this area.

~~Extensive ice penetrating radar has been collected recently over Princess Elizabeth Land (PEL; Fig. 1d), including the eastern part of the Lambert-Amery system (Cui et al., 2020a). This fills in large data gaps from older surveys, and provides the basis for our study. The radar surveys reveal ~1100 km long canyons (Fig. 1) that are incised hundreds of meters deep into the subglacial bed that extend from the Gamburtsev Subglacial Mountains (GSM) to the coast of the Western Ice Shelf (WIS). Li et al. (2021) used airborne magnetic survey collected alongside the radar, which when combined with the radar ice thicknesses and estimated depths at which the bedrock reaches its Currie temperature, can be inverted for geothermal flux. This higher resolution data set (Li et al., 2021) infers a larger heat flux than previous estimates in this region. Furthermore recently discovered subglacial lakes, including potentially the second largest subglacial lake in Antarctica, adds evidence for more widespread basal melting in the region than was thought based on the much sparser earlier survey data (Cui et al., 2020b). The complex subglacial topography, relatively high geothermal heat flux and subglacial lakes imply a complex distribution of basal thermal condition and subglacial water network. This heterogenous basal condition will have shaped much of ice flow and the mass balance of the Lambert-Amery system. This motivates us to investigate how the basal thermal condition inferred from the new high-resolution topography dataset reconciles with surface ice velocities and existing geothermal heat flow maps.~~

Ice temperature is an important factor in the rheology of ice (Budd et al., 2013) and ice flow. Whether the basal ice is at the melting point influences the movement of the ice to a great extent. Ice at the melting point can lead to water flowing along hydraulic gradients and accumulating in local depressions (Fricker et al., 2016). The meltwater lubricates the ice/bed interface or saturates any sediment till layer, allowing higher ice velocities via basal sliding. For instance, the rapid retreat of Thwaites and Pope glaciers in the Amundsen Sea sector of West Antarctica is being facilitated by high heat flow in the underlying lithosphere (Dziadek et al., 2021). ~~flow to a great extent. Ice at the melting point can lead to water lubricating the ice/bed interface or saturating any sediment till layer and facilitating higher ice velocities via basal sliding. This~~This bed-ice linkage forms the basis for making inferences on basal conditions via surface observations (Pattyn, 2010), or relict landforms (e.g. Näslund et al., 2005). ~~Any meltwater will tend to flow along hydraulic gradients, and accumulate in local depressions (Fricker et al., 2016). The ice temperature is controlled by the deformational heat generated from strain within the ice, the lateral advection of heat due to ice motion and the descent rate of ice from the surface, the conduction of heat through the ice and frictional heating from basal sliding.~~

~~Ice sheet models are useful tools to simulate the dynamic evolution of the ice sheet and~~

~~estimate its mass balance.~~The ice temperature is controlled by deformational heat generated from strain within the ice, advection of heat due to lateral ice motion and the descent rate of ice from the surface, conduction of heat through the ice and frictional heating from basal sliding. Ice temperature is hard to evaluate because of the scarcity of in-situ measurements, typically obtained from boreholes that are very rarely drilled through the Antarctic ice sheet. GHF is an important boundary condition for ice temperature simulation, and is generally the largest source of uncertainty. Hence geophysical survey methods are used to indirectly map GHF. To date GHF datasets have been estimated from seismic models (Shapiro and Ritzwoller, 2004; An et al., 2015; Shen et al., 2020), derived from airborne magnetic surveys (Li et al., 2021; Martos et al., 2017) and satellite geomagnetic data (Maule et al., 2005; Purucker, 2013).

~~Large scale studies on the dependence on GHF of the Greenland (Rezvanbehbahani et al., 2019) and Antarctica ice sheet (Pattyn, 2010) have inferred ice and basal temperatures. Regionally, the rapidly retreating Thwaites and Pope glaciers in the Amundsen Sea sector of West Antarctica is being facilitated by the~~Extensive ice penetrating radar data has been collected recently over Princess Elizabeth Land (PEL; Fig. 1d), including the eastern part of the Lambert-Amery system (Cui et al., 2020a). This fills in large data gaps from older surveys, and provides the basis for our study. The radar surveys reveal ~1100 km long canyons (Fig. 1c) that are incised hundreds of meters deep into the subglacial bed that extend from the Gamburtsev Subglacial Mountains (GSM) to the coast of the Western Ice Shelf (WIS). Li et al. (2021) collected airborne magnetic data that can be combined with radar ice thicknesses and estimated depths at which the bedrock reaches its Curie temperature, to invert for the geothermal flux. The resulting higher resolution data set (Li et al., 2021) implies a larger heat flux than previous estimates in this region. Furthermore, recently discovered subglacial lakes, including potentially the second largest subglacial lake in Antarctica, add evidence for more widespread basal melting in the region than was thought based on the much sparser earlier survey data (Cui et al., 2020b). The complex subglacial topography, relatively high geothermal heat flux and subglacial lakes imply a complex distribution of basal thermal conditions and subglacial water networks. These heterogenous basal conditions will have shaped much of the ice flow and mass balance of the Lambert-Amery system. This motivates us to investigate how the basal thermal conditions inferred from the new high-resolution topography dataset can be reconciled with surface ice velocities and existing geothermal heat flow maps.

Ice sheet models can be used to simulate the dynamics and thermodynamics of the ice sheet. Glaciologists have combined ice sheet models with measurements of vertical temperature profiles or thawed basal states to constrain GHF of the ice sheets (e.g. Pattyn, 2010; Rezvanbehbahani et al., 2019). ~~high heat flow in the underlying lithosphere (Dziadek et al., 2021).~~In the Lambert-Amery glacial system, Pittard et al. (2016) suggest that ice flow is most sensitive to the spatial variation in the underlying GHF near the ice divides and along the edges of the ice streams.

In this study, we simulate ice basal temperatures and basal melt rates in the Lambert-Amery system using the new high-resolution digital elevation model, along with six different published GHF maps as forcing for an off-line coupling between a basal energy and water flow model and a 3D full-Stokes ice flow model. We evaluate the quality of the resulting basal temperature field incorporating the Stokes model estimates of ice advection, strain and frictional heating under the different GHF maps using all available observed subglacial lakes and surface velocities. Hence, we make inferences on which GHF maps yield the best match with observations in the region.

2 Regional Domain and Datasets

Our modeled domain is ~~in~~part of the Lambert-Amery system. It consists of two drainage basins: the Lambert Glacier Basin, the American Highland Basin, along with about half of the Amery Ice Shelf (Fig. 1). The 2D domain boundary outlines are defined by the inland ice catchment basin boundary, the central streamline, and the ice front of Amery Ice Shelf. The central streamline was chosen by selecting a point at the confluence of Lambert Glacier and Lepekhin Glaicer and then advecting that point downstream to the ice front using the observed velocity field. The inland sub-basin and the central streamline of the Amery Ice Shelf were chosen as boundaries because the mass flux across them is assumed to be zero by definition.

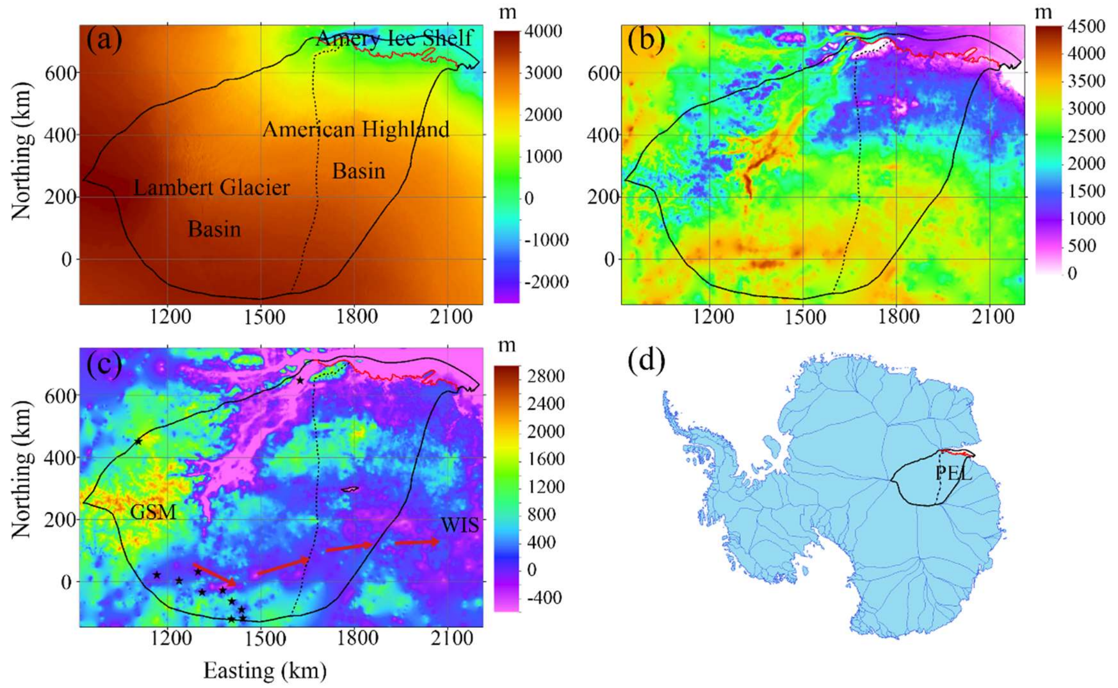

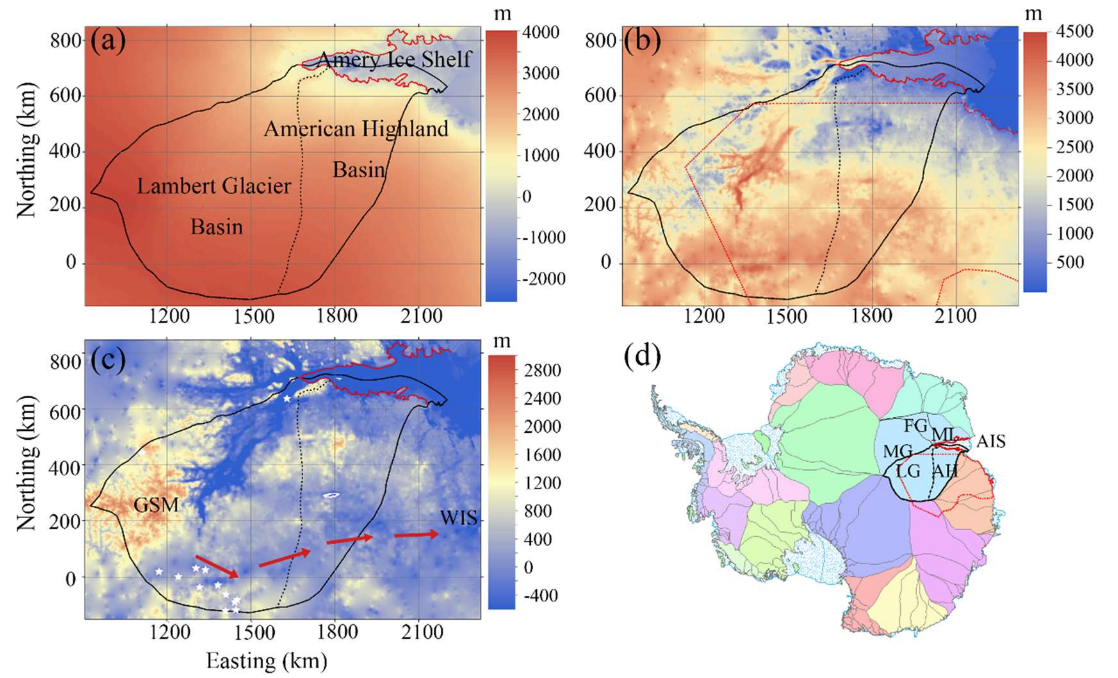

Fig. 1. The domain topography and location with domain boundary overlain. (a) surface elevation; (b) ice thickness; (c) bed elevation; (d) the location of our domain in Antarctica. The solid black curve is the outline of the study domain, including the central streamline of Amery ice shelf and the boundary of inland sub-basins based on drainage-basin boundaries defined from satellite ice sheet surface elevation and velocities (Mouginot et al., 2017; Rignot et al., 2019). The solid red curve is ~~part of~~ the grounding line of Amery ice shelf~~.~~ (Morlighem et al., 2020). The dotted black curve is the dividing line between Lambert Glacier Basin and the American Highland Basin. ~~The black stars in (c) denote the locations of observed subglacial lakes, and the area surrounded by the black line in~~

~~American Highland Basin in (c) is the potentially~~The dotted red curves in (b) and (d) are the boundary of ice thickness data from Cui et al. (2020a), inside which we incorporates data from Cui et al. (2020a). The white stars in (c) denote the locations of observed subglacial lakes (Wright and Siegert, 2012; Cui et al., 2021), and the region within the white line at (1800E, 300N) is potentially the second largest subglacial lake in Antarctic. The red arrows in (c) indicate the routing through the deep subglacial canyon system from GSM to WIS. The sub-basins names of Lambert-Amery system are labeled in (d), ML for MacRobertson Land basin, FG for Fisher glacier basin, MG for Mellor glacier basin, LG for Lambert glacier basin, AH for American Highland basin, and AIS for Amery Ice Shelf.

~~The surface elevation, bedrock elevation, and ice thickness are from MEaSUREs BedMachine Antarctica, version 2 with a resolution of 500 m (Morlighem et al., 2020). Additional ice thickness data from Cui et al. (2020a) were added to further constrain the bed topography beneath the grounded ice (Table 1). The bed elevation is calculated using upper surface elevation minus ice thickness.~~The surface elevation, bedrock elevation, and ice thickness from Cui et al. (2020a) are used in most of the domain (Fig. 1b; Table 1) with additional data are from MEaSUREs BedMachine Antarctica, version 2 at a resolution of 500 m (Morlighem et al., 2020). The bed elevation is calculated by subtraction of the ice thickness from the surface elevation.

The surface ice velocity data are obtained from MEaSUREs InSAR-based Antarctic ice velocity Map, version 2 with resolution of 450 m (Rignot et al., 2017). Data were largely acquired during the International Polar Years 2007 to 2009, and between 2013 and 2016. Additional data acquired between 1996 and 2016 were used as needed to maximize coverage.

Ice sheet surface temperature data are prescribed by ALBMAP v1 with a resolution of 5 km (Le Brocq et al., 2010) and come from monthly estimates inferred from AVHRR data averaged over 1982-2004. Subglacial lake locations are from the fourth inventory of Antarctic subglacial lakes (Wright and Siegert, 2012), with the addition of the newly discovered lakes (Cui et al., 2020b).

Six GHF datasets (Fig. 2; Table 2) are used in this study. All the datasets are interpolated into the same 2.5 km resolution.

Table 1 Datasets used in this study.

Variable name	Dataset	Resolution	Reference
surface elevation, bedrock elevation, and ice thickness	MEaSUREs BedMachine Antarctica version 2	500 m	Morlighem et al., 2020; Cui et al., 2020
surface ice velocity	MEaSUREs InSAR-based Antarctic ice velocity Map, version 2	450 m	Rignot et al., 2017
surface temperature	ALBMAP v1	5 km	Le Brocq et al., 2010;
subglacial lakes location	The fourth inventory of Antarctic subglacial lakes	-----	Wright and Siegert, 2012; Cui et al., 2021

Table 2 The six GHF datasets used in this study.

GHF map	Reference	Method	Mean (mW m^{-2})	Range (mW m^{-2})
Martos	Martos et al., 2017	airborne geomagnetic data	72	47-90
Shen	Shen et al., 2020	seismic model	50	43-59
An	An et al., 2015	seismic model	55	40-66
Shapiro	Shapiro and Ritzwoller, 2004	seismic model	54	45-58
Purucker	Purucker, 2013	Satellite geomagnetic data	47	26-47
Li	Li et al., 2021	airborne geomagnetic data	72	52-90

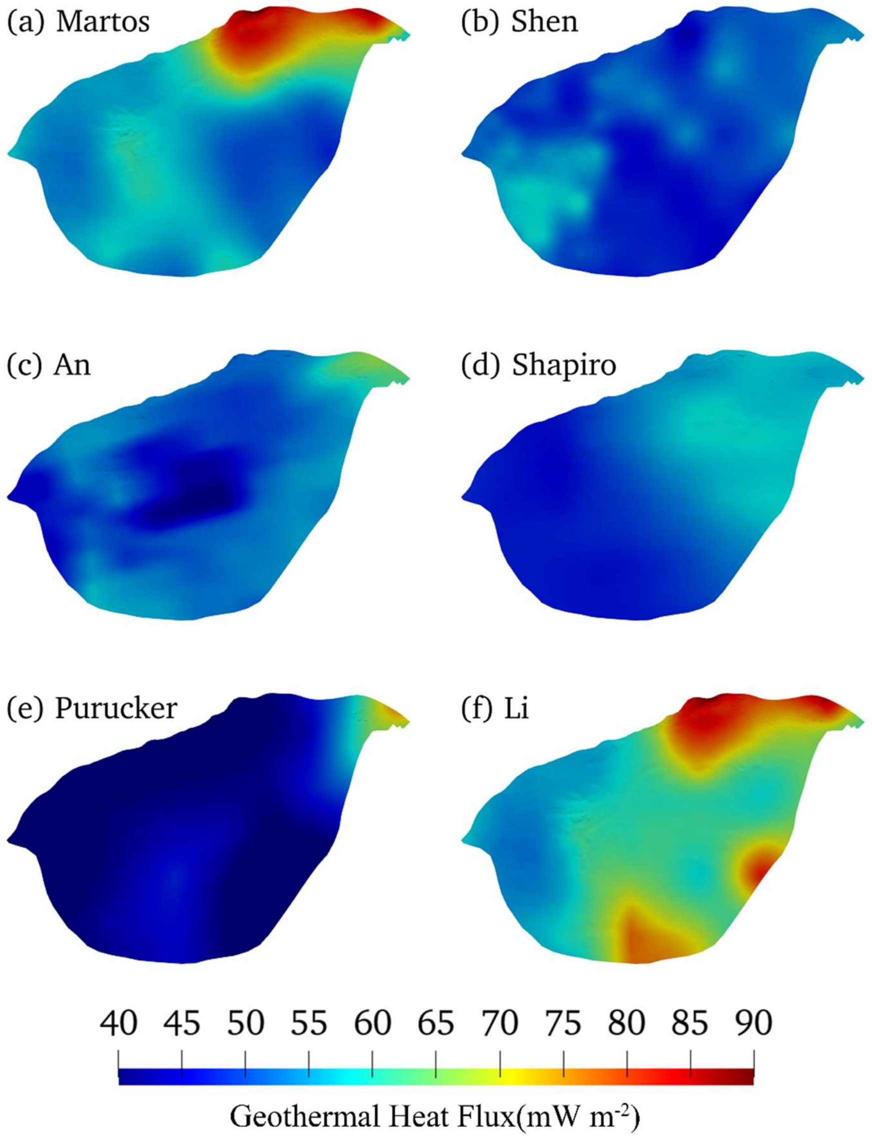

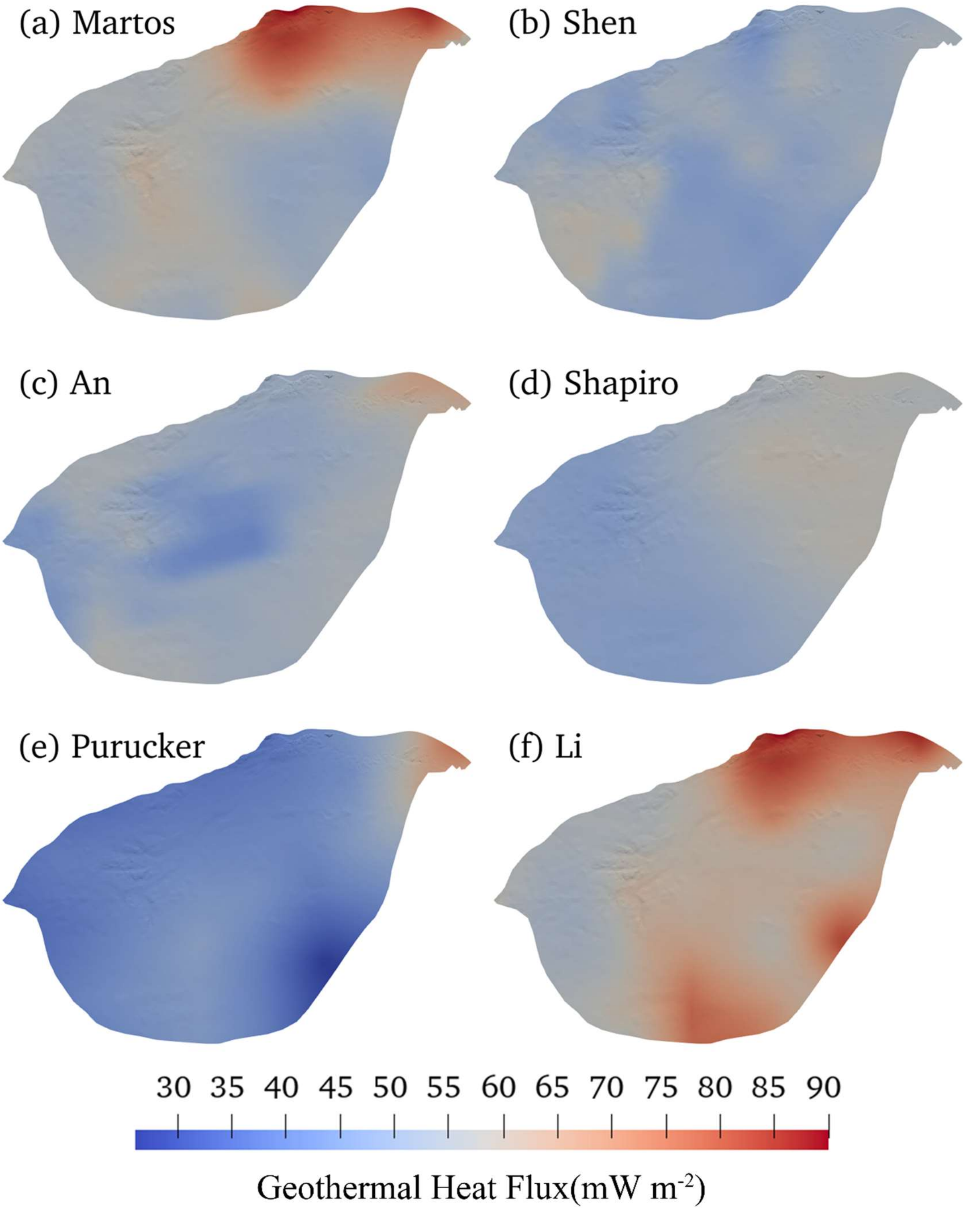

Fig. 2. The spatial distribution of GHF over our domain as described in Fig. 1. See Table 2 for the GHF map details.

3 Model

Our goal is to infer the basal thermal ~~condition~~conditions, including basal temperature and basal melt rate in the domain. Geothermal heat flux, ~~internal~~englacial heat conduction and basal friction heat are the main heat sources that ~~determines~~determine the basal thermal ~~condition~~conditions. Therefore, we need to model both ice flow velocity and stress for basal friction heat and ice temperature for ~~internal~~englacial heat conduction.

We ~~use~~solve an inverse ~~method implemented in~~ problem by a full-Stokes model, implemented in Elmer/Ice, to ~~estimate ice flow velocity and stress,~~ infer the basal friction coefficient ~~and~~such that the modelled velocity best fits observations (Gagliardini et al., 2013). Using the best-fit basal friction coefficient, we obtain the ice flow velocity, stress and basal friction heat. A proper initial ice temperature is needed in solving the inverse ~~method~~problem. To get it, we use a forward model that consists of an improved Shallow Ice Approximation (SIA) thermomechanical model with a subglacial hydrology model (Wolovick et al., ~~2021~~2021a). The forward model uses the modelled velocity direction and basal slip ratio from the full-Stokes inverse model to constrain its solution. We do steady state simulations by coupling the two models. We will describe the forward model in Section 3.1 and the inverse model in Section 3.2, then the coupling in Section 3.3.

3.1 Forward Model

The forward model consists of a thermomechanical steady state model using an improved Shallow Ice Approximation (SIA) in equilibrium with the subglacial hydrological system (Wolovick et al., ~~2021~~2021a)~~, described in Sections 3.1.1-3.1.3.~~. It has internal consistency between three components: ice flow, ice temperature, and basal water flux. The numerical model requires three coupled components to be consistent with one another: (1) ~~Integration~~integration for balance flux and englacial temperature downhill in the ice surface, (2) ~~Integration~~integration for basal water flux and freezing rate downhill in the hydraulic potential, and (3) ~~Rheology~~rheology and shape function computations to determine the distribution of ice flux and shear heating. ~~These three components are solved within a large fixed-point iteration. In our coupling scheme, components (1) and (3) are constrained by the velocity direction and basal sliding ratio computed by the full-Stokes inverse model.~~ The model performs a fixed-point iteration for consistency between these three components. In addition. we improve on the model used in Wolovick et al. (2021a) by combining the observed velocity field, the velocity field from the full-Stokes model, and the surface gradient direction to compute a merged flow direction field for step (1). The observations are used where flow is fast, Elmer/Ice modelled velocity is used where flow is slow, and the surface gradient is only used near the margins of the domain where the Elmer velocity field is not reliable (Fig. 3). The simulation is done on a finite difference mesh with resolution of 2.5 km.

~~3.1.1 Balance Flux and Thermal Model~~

The ~~mass balance of the ice sheet is given by,~~

$$\cancel{\nabla \cdot (\bar{u}H) = a - m,} \qquad \cancel{(1)}$$

~~where $\bar{u}$ is the vertically averaged horizontal velocity, H is the ice thickness, a is~~ surface accumulation rate ~~and m is basal melt rate, both expressed as ice equivalent~~

~~thickness per unit time. In most of the domain, the direction of the horizontal velocity vector is taken from the full-Stokes Elmer/Ice model, but the magnitude of horizontal velocity is allowed to vary to ensure exact mass conservation for a given surface accumulation rate and basal melt forcing. Near the domain edges the velocity direction in Elmer/Ice is unreliable, and the smoothed surface gradient is~~ we used ~~to provide velocity direction at those locations instead. The magnitude of horizontal velocity is determined using a balance flux algorithm (e.g., Budd and Warner, 1996). The integration order is taken from the smoothed ice surface elevation, with local corrections to ensure that no grid cells depend on values downstream of themselves. Once the column-average horizontal velocity in a given grid cell is known, the vertical distribution of horizontal velocity in the ice column is calculated by:~~

~~$\boldsymbol{u}(x,y,z) = \bar{u}(x,y)\hat{u}(x,y,z),$ (2)~~

~~where $\boldsymbol{u} = (u_x, u_y)$ is the horizontal velocity vector and $\hat{u}$ is a dimensionless scalar shape function for horizontal velocity (section 3.1.3). The shape function is taken from the last iteration and interpolated to the edge of the mesh. Once the vertical distribution of horizontal velocity is known, the vertical velocity is calculated from the incompressibility condition by,~~

~~$w(z) = -m - \int_0^z \nabla \cdot \boldsymbol{u}\, dz',$ (3)~~

~~where w is the vertical component of velocity.~~

~~After obtaining all the three components of the velocity, the ice column temperature can be calculated from the conservation of energy,~~

~~$-\frac{d}{dz}\left(k(T)\frac{dT}{dz}\right) + \rho_i \vec{u} \cdot \nabla\left(c_{p,i(T)}\mathrm{T}\right) = 4\eta\dot{\epsilon}_E^2,$ (4)~~

~~where T is temperature, $k(T)$ is the temperature-dependent~~in the forward thermal ~~conductivity of ice, ρ_i is the density of ice, $c_{p,i(T)}$ is the temperature-dependent specific heat capacity of ice, $\vec{u}$ is the full (3-component) velocity vector, η is the ice viscosity and $\dot{\epsilon}_E$ is the effective strain rate.~~model is the mean of Arthern et al. (2006) and Van de Berg et al. (2005). Both were accessed through the ALBMAP_v1 dataset (Le Brocq et al., 2010).

~~For the~~ One key complexity is how to deal with basal thermal boundary condition~~, at the surface, we use the Dirichlet condition where the temperature is equal to the surface temperature.~~. At the bottom of ice shelves, we set basal temperature ~~as~~equal to the pressure melting point. At the bed of grounded ice, the boundary condition can be either Dirichlet or Neumann condition depending on the basal melting and subglacial water conditions. The ~~logical~~basal boundary conditions are given by,

~~$k(T)\frac{dT}{dz} = G, \quad \text{for } T < T_m \text{ and } m = 0;$ (5)~~

~~$\mathrm{T} = T_m, \quad \text{for } m \neq 0,$ (6)~~

~~Where~~

$$-k(T)\frac{dT}{dz} = G, \quad \text{for } T < T_m \text{ and } m = 0; \qquad (1)$$

$$T = T_m, \quad \text{for } m \neq 0, \tag{2}$$

where T_m is the pressure-dependent melting temperature, G is GHF, taking six GHF datasets listed in Table 2. The thermal condition will switch from Neumann (Eq ~~5~~1) to Dirichlet (Eq ~~6~~2) if the basal temperature exceeds the pressure-dependent melting point. The opposite switch from Dirichlet to Neumann is determined by the hydrology model, if there is insufficient water input to supply a large freezing rate. ~~The basal melt rate here can be either positive or negative representing melting or freezing; when it is negative, the freezing must be balanced by an influx of water.~~

~~The thermally determined melt rate is,~~

$$\cancel{\rho_i L m = G - k(T)\frac{dT}{dz} + \vec{u}_b \tau_b - \overrightarrow{q_w} \cdot \left(\nabla\phi + \rho_w c_{p,w} \beta \nabla P\right),} \tag{7}$$

~~where L is the latent heat of fusion, $\overrightarrow{q_w}$ is the flux of water along the basal plane, $\phi = \rho_i g H + \rho_w g B$ is the hydraulic potential, ρ_w is the density of water, $c_{p,w}$ is the specific heat of water, β is the pressure coefficient of the melting point, and $P = \rho_i g H$ is the overburden pressure of the ice sheet. The final term in Eq 7 represents the combined effect of viscous dissipation and sensible heat changes within the water system and can potentially give rise to glaciohydraulic supercooling.~~

~~3.1.2 Basal Hydrology Model~~

~~The water flux is determined from mass conservation,~~

$$\cancel{\nabla \cdot \overrightarrow{q_w} = \frac{\rho_i}{\rho_w} m,} \tag{8}$$

~~where we have included the density ratio to convert melt rate from ice-equivalent thickness to water-equivalent thickness. The water flux is computed in a similar style of balance flux calculation as the ice flux, where the flux vector is assumed to point downhill in hydraulic potential and Eq 8 is integrated downhill to determine flux magnitude. The water flow is governed by hydraulic potential ϕ. We fill closed basins in the hydraulic potential before running the model to ensure that we have a continuous flow path all the way to the margins of the domain. As long as water flux magnitude remains positive (that is, directed down-potential), the hydrology model uses the thermally determined melt/freeze rate from Eq 7. In the event that the balance flux calculation would yield negative water flux (that is, water flow directed up-potential), the hydrology model switches the grid cell from Dirichlet back to Neumann, and the limiting freezing rate is determined by rearranging Eq 8 to solve for the value of m that results in zero flux leaving the grid cell. In grid cells that receive no water input from upstream, this merely means that the melt/freeze rate is set to zero and the basal boundary condition can be given by Eq 5 without complication, but for grid cells at the termination of a water network, a special partially frozen condition must be used.~~

~~When a water network terminates by freeze-on, we have grid cells in which the freezing front penetrates partially through the grid cell but not completely. To respect both mass and energy conservation, it is necessary for there to be a nonzero freezing rate and nonzero water flux entering these grid cells despite the fact that their average~~

temperature is below the melting point. For these partially frozen cells, the freezing rate is determined by the water supply through Eq 8 as described above. That freezing rate is associated with a release of latent heat, which must be accounted for by the thermal model. The hydrology model, therefore sets these grid cells to a Neumann condition, but instead of being taken from Eq 5, the basal temperature gradient is determined by rearranging Eq 7 to solve for $\frac{dT}{dz}$. The basal temperature in these grid cells is thus not fixed to the melting point, but it nonetheless is higher than it otherwise would be because of the release of latent heat at the termination of the water network.

3.1.3 Rheology and Shape Function Model

The shape function determines the distribution of horizontal velocity with depth. The effective viscosity of the ice is given by,

$$\eta = \frac{1}{2}(\mathrm{A(T)})^{-\frac{1}{n}} \dot{\varepsilon}_E^{\frac{1-n}{n}}, \qquad (9)$$

where $A(T)$ is the temperature-dependent rate factor calculated using an Arrhenius equation (Cuffey and Paterson, 2010),

$$A(T) = A_0 \exp\left(\frac{-Q}{RT}\right), \qquad (10)$$

where A_0 is the prefactor, Q is the activation energy, R is the universal gas constant. $n = 3$ is the rheological exponent for ice. The effective strain rate $\dot{\varepsilon}_E$ is given by,

$$\dot{\varepsilon}_E = \sqrt{\dot{\varepsilon}_{xy}^2 + \dot{\varepsilon}_{xz}^2 + \dot{\varepsilon}_{yz}^2 + \frac{1}{2}\left(\dot{\varepsilon}_{xx}^2 + \dot{\varepsilon}_{yy}^2 + \dot{\varepsilon}_{zz}^2\right)}. \qquad (11)$$

Once we have the viscosity, we can compute the shape function. We use the results of the full-Stokes inverse model to constrain the slip ratio, $\hat{u}_b = u_b/\bar{u}$. We then assume the shear stress between the bed and the surface varies linearly, and then use the relationship between stress and strain rate to get the vertical gradient of horizontal velocity, $\frac{du}{dz} = \sigma_b \frac{1-\hat{z}}{\eta}$. Integrating this expression up from the bed, normalizing to unit amplitude, and canceling the common factor, we get the shape function,

$$\hat{u}(\hat{z}) = \hat{u}_b + (1 - \hat{u}_b)\frac{\int_0^{\hat{z}} \frac{1-\hat{z}'}{\eta(\hat{z}')} d\hat{z}'}{\int_0^{1} \frac{1-\hat{z}'}{\eta(\hat{z}')} d\hat{z}'}, \qquad (12)$$

where $\hat{u} = u/\bar{u}$ is the shape function for horizontal velocity, $\hat{z} = (z - B)/H$ is normalized elevation.

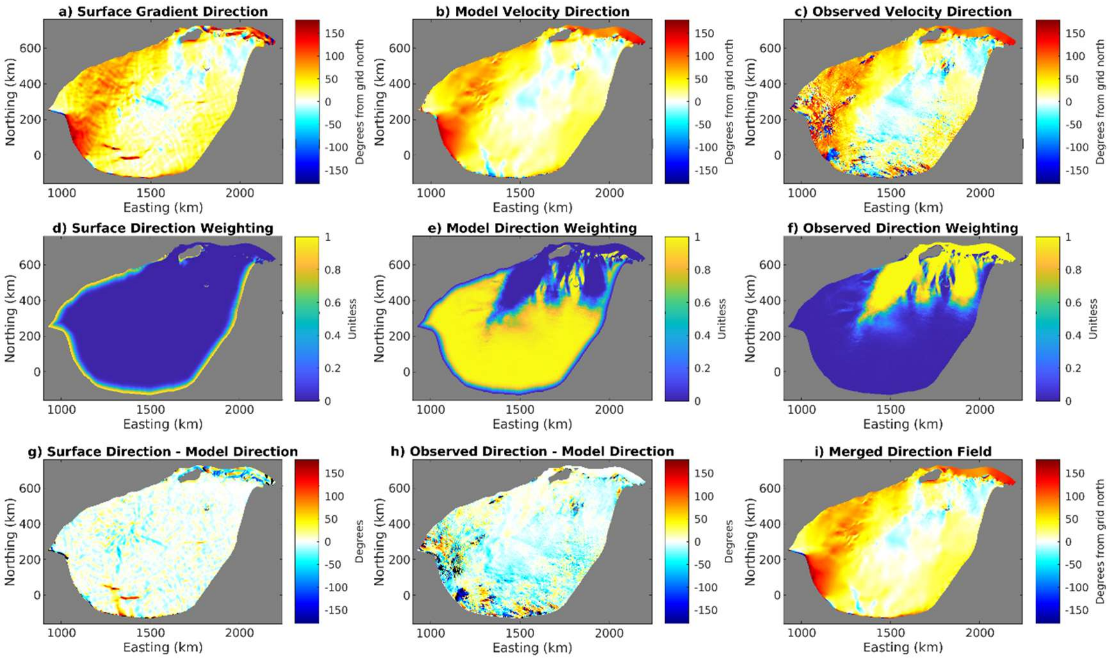

Fig. 3. Velocity direction fields, in degrees clockwise from grid north. The first row shows the direction from surface gradient (a), Elmer/Ice modelled velocity (b), and the observed velocity direction (c). The middle row (d-f) shows the 3 corresponding weighting fields (the sum of these weights is 1). The bottom row shows the difference between the direction of surface gradient and Elmer/Ice modelled velocity (g), the difference between the observed velocity direction and Elmer/Ice modelled velocity h), and the merged velocity field used in the forward model (i).

One improvement on the method from Wolovick et al. (2021a) is that a temperate basal ice layer with non-zero thickness is permitted in our model in the case that the modelled basal ice temperature reaches the pressure melting point. We do this using a weak-form solution in which the volumetric englacial melt rate rises steeply as temperature exceeds the melting point. The englacial melting absorbs latent heat and serves to limit temperature rise. We parameterize the increase in volumetric melt rate as an exponential function of temperature with a 1 K e-folding temperature, and a prefactor given by the englacial strain heating and the latent heat of fusion. All englacial meltwater generated this way is assumed to immediately drain to the bed.

Another key component of the forward model is the shape function determining the distribution of horizontal velocity with depth. We also improve the shape function in Wolovick et al. (2021a) by adding basal slip ratio, $\hat{u}_b = u_b/\bar{u}$, where u_b is the basal velocity magnitude and $\bar{u}$ is the vertically averaged horizontal velocity magnitude. The slip ratio is taken from the full-Stokes inverse model. Other than the addition of a spatially variable slip ratio, the shape function calculation is unchanged from Wolovick et al. (2021a).

3.2 Inverse ~~Method~~Model with full-Stokes Model

The spatial distribution of basal friction in the domain is modelled by solving an inverse ~~method~~problem using the three-dimensional the full-Stokes model, Elmer/Ice, an open source finite element method package(Gagliardini et al., 2013). The inverse ~~method~~model is based on adjusting the spatial distribution of the basal friction coefficient to minimize the misfit between simulated and observed surface velocities. The modelled velocity is obtained by solving the full-Stokes equation, which includes conservation equations for both the momentum and mass of the ice,

$$\cancel{div\ \boldsymbol{\tau} - gradp = \rho_t g,} \qquad \cancel{(13)}$$

$$\cancel{div\ \vec{v} = 0,} \qquad \cancel{(14)}$$

$$div\ \boldsymbol{\tau} - gradp = \rho_i \vec{g}\ , \qquad (3)$$

$$div\ \vec{v} = 0, \qquad (4)$$

where ~~τ~~$\boldsymbol{\tau}$ is the deviatoric stress tensor, p is the isotropic pressure, ρ_i is ice density, ~~g~~ $\vec{g}$ is the acceleration due to gravity (0, 0, -9.81) m·s^{-2}, $\vec{v}$ ~~$= (u, v, w)$~~ is ice velocity. According to Glen's flow relation, deviatoric stress is related to the deviatoric part of the strain rate tensor, $\dot{\varepsilon_E}$, which can be described by ~~τ~~$\boldsymbol{\tau} = 2\eta\dot{\varepsilon_E}$, where ~~$\eta$ denotes ice~~the effective viscosity~~, given by Eq 9~~ of the ice, η, is sensitive to the temperature-dependent flow rate factor $A(T)$ ~~given by Eq 10. Ice~~calculated using an Arrhenius equation (Cuffey and Paterson, 2010). The ice temperature distribution ~~is~~comes from the ~~modelled result of~~ forward model in section 3.1.

3.2.1 Mesh Generation and Refinement

Firstly, we use GMSH (Geuzaine and Remacle, 2009) to generate an initial 2-D horizontal footprint mesh with the boundary described in section 2. Then we refine the mesh by an anisotropic mesh adaptation code called the Mmg library (http://www.mmgtools.org/). The resulting mesh is shown in Fig. ~~3~~4 and has minimum and maximum element sizes of approximately 1000 m and 8000 m. The 2-D mesh is then vertically extruded using 10 equally spaced, terrain following layers.

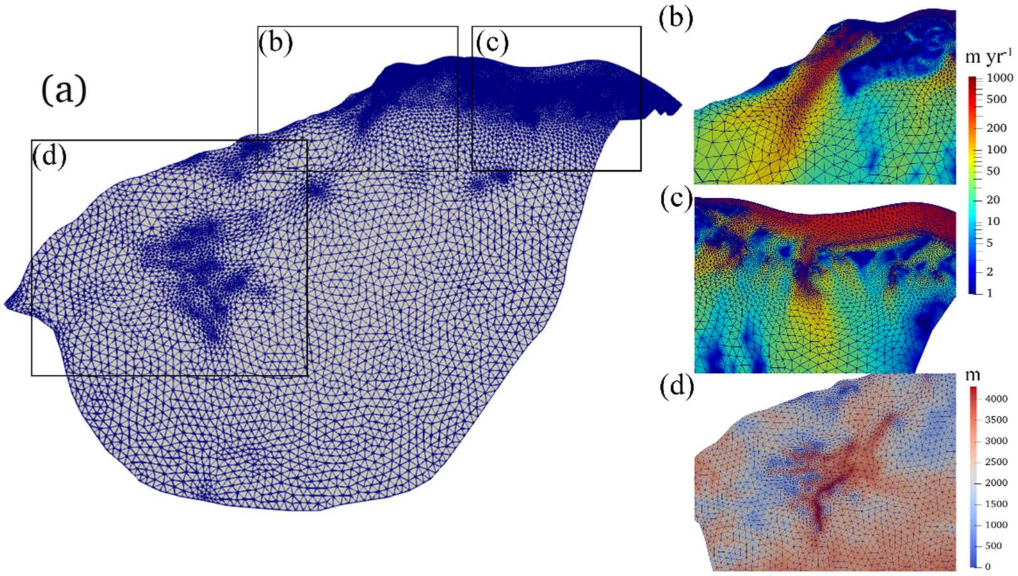

Fig. ~~3.~~4. The refined 2-D horizontal domain footprint mesh (a). Boxes outlined in (a) are shown in detail overlain with surface ice velocity in (b) and (c), and with ice thickness in (d).

3.2.2 Boundary Condition

The ice surface is assumed to be stress-free. At the ice front, the normal stress under the sea surface is equal to the hydrostatic water pressure. On the lateral boundary, the normal stress is equal to the ice pressure applied by neighboring glaciers and the normal velocity is assumed to be 0. The bed for grounded ice is assumed to be rigid, impenetrable, and fixed over time. Since we perform a stress-balance snapshot in the full-Stokes model, we do not need to prescribe surface mass balance or basal mass balance in the boundary conditions.

The normal basal velocity is set to 0 at the ice-bed interface. The ~~Weertman~~linear sliding law is used to describes the relationship between the basal sliding velocity,~~u_b~~ $\vec{u}_b$, and the basal shear force, ~~τ_b,~~ $\vec{\tau}_b$, on the bottom of grounded ice,

$$\cancel{\tau_b = C\, \vec{u}_b. \qquad (15)}$$

$$\vec{\tau}_b = C\, \vec{u}_b. \qquad (5)$$

To avoid non-physical negative values, $C = 10^{\beta}$ is used in the simulation. We call β the basal friction coefficient rather than C. ~~C~~C is initialized to a constant value of 10^{-4} MPa m^{-1} yr (Gillet-Chaulet et al., 2012), and then replaced with the inverted C in subsequent inversion steps.

3.2.3 Surface Relaxation

We relax the free surface of the domain by a short transient run to reduce the non-physical spikes in initial surface geometry (Zhao et al., 2018). The transient simulation period here is 0.5 yr with a timestep of 0.01 yr.

3.2.4 Inversion and Improvement for Basal Friction Coefficient

Taking the results from the surface relaxation as ~~initial condition,~~our ice geometry we use an inverse ~~method~~model to retrieve the basal friction coefficient, the deviatoric stress field and ice velocity field. The inverse ~~method is to adjust~~model adjusts the basal friction coefficient C to minimize the value of the cost function (Morlighem et al., 2010), which is defined as the difference between the simulated surface velocity and the observed,

$$\cancel{J_0 = \int_{\Gamma_S} \frac{1}{2}(|u| - |u^{obs}|)^2 d\Gamma, \qquad (16)}$$

$$J_0 = \int_{\Gamma_s} \frac{1}{2}(|\vec{u}| - |\vec{u}_{obs}|)^2 d\Gamma \qquad (6)$$

where Γ_S is the ice surface, ~~u~~ $\vec{u}$ and ~~u^{obs}~~ $\vec{u}_{obs}$ are the simulated and observed surface velocities.

To avoid over-fitting of the inversion solution to non-physical noise in the observations, a regularization term,

$$\cancel{J_{reg} = \frac{1}{2}\int_{\Gamma_S}\left(\left(\frac{\partial C}{\partial x}\right)^2 + \left(\frac{\partial C}{\partial y}\right)^2\right) d\Gamma, \qquad (17)}$$

is added to the cost function, then the total cost function is defined as,

$$\cancel{J_{tot} = J_0 + \lambda J_{reg}, \qquad (18)}$$

where λ is a positive regularization weighting parameter. An L-curve analysis (Hansen and Johnston, 2000) has been done for inversions to find the optimal λ by plotting the term J_{reg} as the function of J_0. The optimal value of 10^{10} is chosen for λ to minimize J_0.

Basal friction in reality depends on basal temperature, i.e., it is relatively large on cold beds since the ice is frozen, and small on warm bed where basal temperature reaches pressure-melting point allowing the ice to slide (Greve and Blatter, 2009). However, in the inverse model, basal friction coefficient (Eq 5) is adjusted to match velocity observations without regard to basal temperature, which leads to unrealistic noise manifested as local spikes in modelled basal friction heat (Fig. 5a).

We improve the parameterization of β via C in Eq 5 (Section 3.2.2) by considering basal temperature T_{bed},

$$\beta_{new} = \beta_{old} + \alpha(T_M - T_{bed}), \qquad (9)$$

where β_{old} is that from by the inverse model, α is a positive factor to be tuned, T_M is pressure-dependent melting temperature. β_{new} equals β_{old} at a bed with temperate ice, and is larger than β_{old} at a bed with ice temperature lower than T_M. We tune α in the range of [0.1, 2] with an interval of 0.1, and find the local spikes in modelled friction heat become fewer (Fig. 5) as α increases from 0.1 to 1, but stay almost constant with α from 1 to 2. Therefore, we take α to be 1, and use the parameterization of β_{new} in Eq

5 in all the simulations. Using Eq 9, the difference of simulated and observed surface velocity is unchanged over the region except for some parts of the inland boundary.

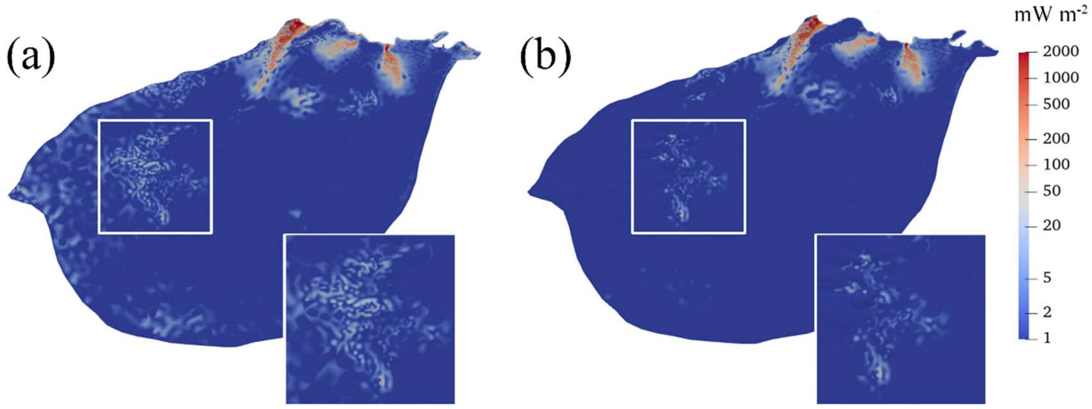

Fig. 5. Comparison of modelled basal friction heat with basal friction coefficient β_{old} (a) and β_{new} with α=1 (b). The white square is enlarged.

3.2.5 Basal Melt Rate

Based on the inverted basal velocity and basal shear ~~force~~stress, we can calculate the basal friction heat. ~~Then we can~~We then produce the basal melt rate using the thermal equilibrium as follows~~:~~ (Greve and Blatter, 2009):

$$\cancel{M = \frac{G+\vec{u}_b\vec{\tau}_b-k(T)\frac{dT}{dz}}{\rho_i L},} \quad \cancel{(19)}$$

~~where M is the basal melt rate.~~

$$M = \frac{G+\vec{u}_b\vec{\tau}_b+k(T)\frac{dT}{dz}}{\rho_i L}, \quad (10)$$

where M is the basal melt rate, G is GHF, $\vec{u}_b\vec{\tau}_b$ is the basal friction heat, $-k(T)\frac{dT}{dz}$ is the upward heat conduction, ρ_i is the ice density, and L is latent heat of ice melt. The ice-bed interface gets heat through GHF and friction heat but loses heat from upward heat conduction.

~~4 Simulations and Results~~

~~4.1~~3.3 Experimental Design of coupled simulations

We design the coupled simulations ~~by~~in an 8-step scheme ~~by~~for coupling the forward model and inverse model~~:~~ similar as Zhao et al. (2018):

1. We run the forward model with the velocity direction taken from a mixture of the surface gradient and surface velocity observations, and get an initial modelled englacial temperature.
2. We do surface relaxation in Elmer/Ice with the englacial temperature from step

1.

3. Taking the results from step 2 as the initial state, we do an inversion ~~simulation by~~in Elmer/Ice using the modeled englacial temperature from step 1, to get a modelled surface velocity best fit to the observed surface velocity. The modelled surface velocity will remove some artifacts in the observed field.
4. We run the forward model using the velocity directions ~~from~~ derived by merging the Elmer~~-~~/Ice~~,~~ modelled velocity, the surface gradient and the surface velocity observations. We use the modelled velocity by the full-Stokes inverse model to constrain the basal slip ratio, then constrain rheology and shape function in the forward model. Then we get an updated modelled englacial temperature.
5. We run the inverse ~~method~~model in Elmer/Ice with the improved englacial temperature from step 4, and get an updated modelled velocity.
6. We run the forward model again using the ratio of basal sliding to column-average velocity in Elmer/Ice from step 5 to constrain the slip ratio, and get a further updated basal temperature.
7. We run the inverse ~~method~~model again in Elmer/Ice with the improved englacial temperature from step 6, and get an updated modelled velocity and stress.
8. We analyze the modelled results in step 7, calculate basal friction heat and basal melt rate.

We ~~use~~perform the above procedure for all six sets of GHF ~~in~~ to produce six different results for the basal thermal ~~condition in the forward model, and obtain six sets of englacial temperature used in the inverse model. Correspondingly, we call the six experiments: Martos, Shen, An, Sr, Purucker and Li~~conditions.

4~~.2 Improvement of Basal Friction Coefficient~~

~~Basal friction in reality depends on basal temperature, i.e., it is relatively large on cold beds since the ice is frozen, and small on warm bed where basal temperature reaches pressure-melting point allowing the ice to slide. However, in the inverse model, basal friction coefficient (Eq 15) is adjusted to match velocity observations without regard to basal temperature, which leads to unrealistic noise manifested as local spikes in modelled basal friction heat .~~

~~We improve the parameterization of β via C in Eq 15 (Section 3.2.2) by considering basal temperature T_{bed},~~

~~$\beta_{new} = \beta_{old} + \alpha(T_M - T_{bed}),$ (20)~~

~~where β_{old} is modelled by inverse model, α is a positive factor to be tuned, T_M is pressure-dependent melting temperature. β_{new} equals β_{old} at a warm bed with temperate ice, and is larger than β_{old} at a cold bed with ice temperature lower than T_M. We tune α in the range of [0.1, 2] with an interval of 0.1, and find the local spikes in modelled friction heat become less as α increases from 0.1 to 1, and keep almost the same with α from 1 to 2. Therefore, we take α to be 1, and use the parameterization of β_{new} in Eq 20 in all the simulations. Using Eq 20 does not change the modelled surface~~

~~velocity in the interior region.~~

~~4.3~~ Simulation Results

4.~~3.~~1 Ice Velocity

In the inverse ~~method,~~model, the misfit between the modeled ~~the surface velocity matches best to~~ and the observed surface velocity~~.~~ is minimized. Therefore, we get very similar distributions of modeled surface velocity field using different GHFs. Fig. ~~4~~6 shows the modelled velocity in the ~~Martos~~ experiment using Martos et al. (2017) GHF as an example. The modeled surface velocity shows spatial similarities to the observed surface velocity (Fig. ~~4a~~6a, b). Three fast-flowing outlet glaciers (Lambert Glacier, Lepekhin Glacier and Kronshtadtskiy Glacier) deliver ice to the ice shelf. The velocity of the Lambert glacier exceeds 800 m yr^{-1} at the grounding line. The Lepekhin Glacier and the Kronshtadtskiy Glacier have maximum flow velocities of about 200 and 400 m yr^{-1} at their grounding lines, respectively. Regions with large differences between modeled and observed surface velocity occupy a small fraction of the whole area (Fig. ~~4c~~6c) and are associated with high velocity gradients. Ice velocity decreases with depth. Fig. ~~4d~~6c shows modeled basal ice velocity. The maximum basal velocity on Lambert Glacier exceeds 500 m yr^{-1} near the grounding line, and maximum basal velocities on Lepekhin Glacier and the Kronshtadtskiy Glacier reach about 150 and 200 m yr^{-1} at the grounding line.

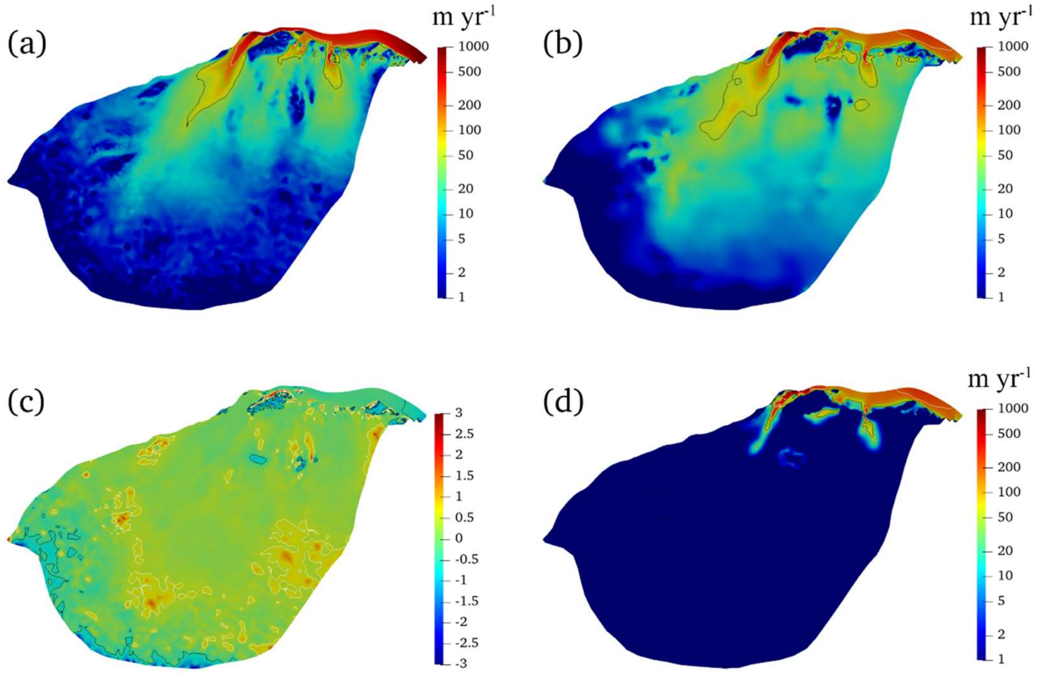

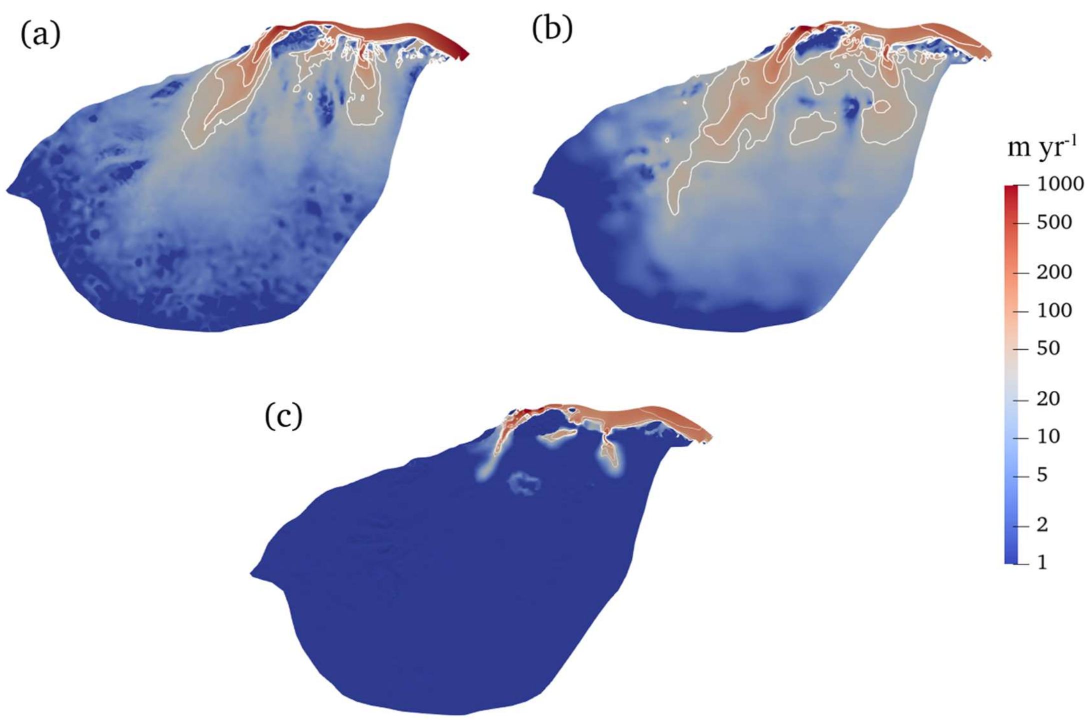

Fig. ~~4.~~6. (a) Observed surface velocity, (b) modeled surface velocity in the ~~Martos~~ experiment using Martos et al. (2017) GHF, (c) ~~difference of modeled and observed surface velocity plotted as log$_{10}$(modeled/observed), (d)~~ modeled basal velocity. The ~~black, cyan and~~ white solid lines in (a), (b), and (~~d~~c) represent speed contours of 30, 50, 100 and 200 m yr^{-1}, respectively. ~~The white lines in (c) represent contours of 0.5, and the black lines represent contours of -0.5.~~ The three fast-flowing outlet glaciers in plot (a) from left to right are Lambert, Lepekhin and Kronshtadtskiy glaciers.

4~~.3~~.2 Basal Ice Temperature and Heat Conduction

In Fig. ~~5~~7 we show the modelled basal temperature from the six experiments. ~~There~~The modelled ice basal temperatures in the fast-flowing regions are all at the pressure melting point (“warm”). However, there are significant differences in the modelled distribution of warm ~~base (basal temperature reaching the pressure melting point)~~-based conditions in the slow-flowing region using different GHFs. The basal temperature is highly dependent on the GHF. In the ~~Li~~ experiment using Li et al. (2021) GHF (Fig. 7f), which has ~~high~~the highest GHF ~~over~~within the domain, the basal ~~temperatures~~ temperature is at the melting point over most of the domain ~~reaches the melting point, and the area of warm base is the largest. The Martos~~ , with extensive cold based regions confined to the southern part. The experiment ~~with~~ using Martos et al. (2017) GHF (Fig. 7a), which has the second ~~high~~highest GHF, yields the second largest area of warm base, and the ~~Purucker~~ experiment using Purucker (2013) GHF (Fig. 7e), with the ~~coldest~~lowest GHF gives the smallest warm-based area which is concentrated around the fast-flowing ice. All experiments display cold basal temperatures ~~at~~to the southwest of the Lambert Glacier Basin, ~~where there are~~ associated with thin ice over subglacial mountains~~.~~ (Fig. 1c).

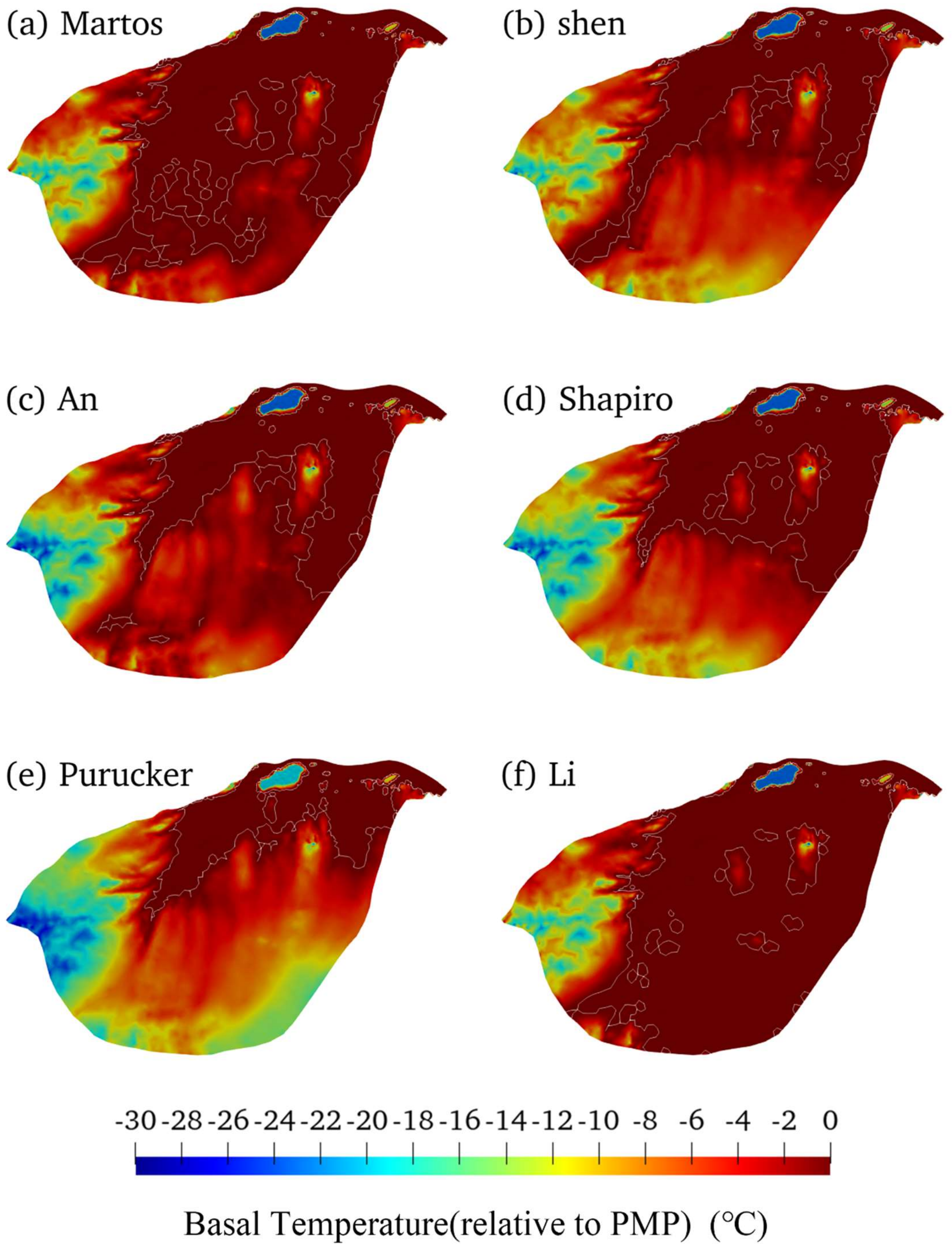
(a) Martos
(b) shen
(c) An
(d) Shapiro
(e) Purucker
(f) Li
-30 -28 -26 -24 -22 -20 -18 -16 -14 -12 -10 -8 -6 -4 -2 0
Basal Temperature(relative to PMP) (°C)

595

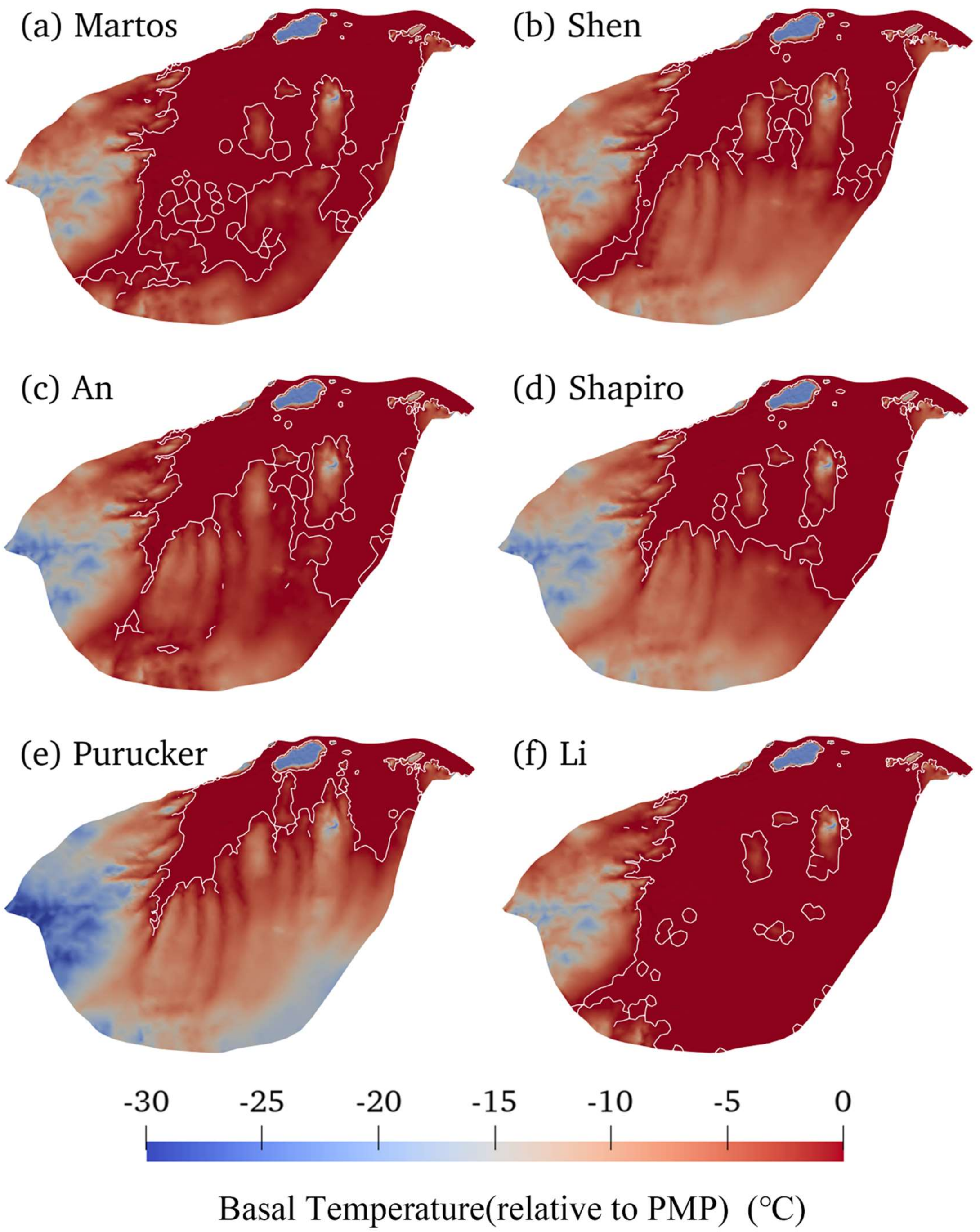

Fig. ~~5.~~7. Modelled basal temperature relative to pressure melting point, (a) to (f) corresponding to the GHF (a) to (f) in Fig. 2. The ice bottom at the pressure-melting point is delineated by a white contour.

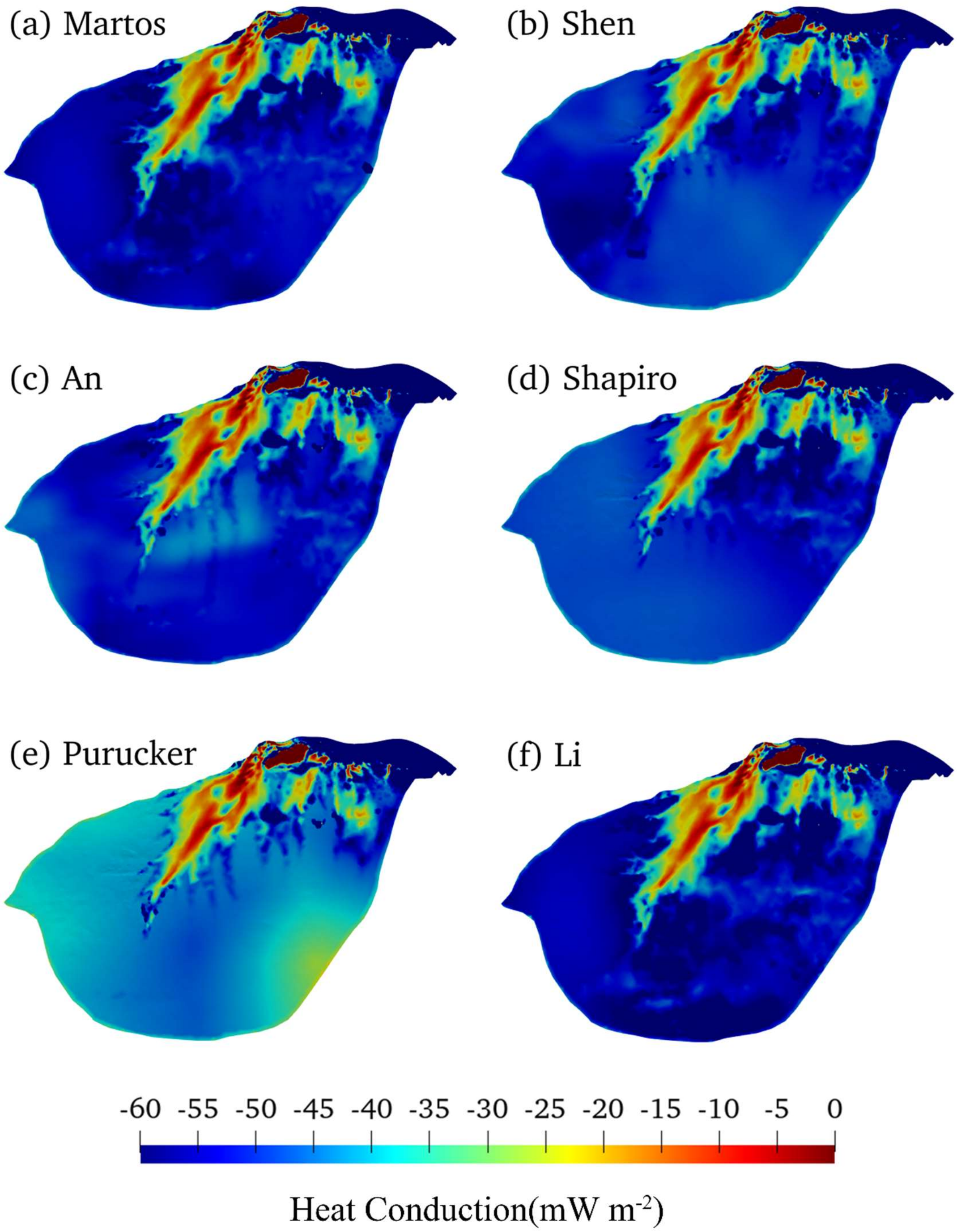
(a) Martos
(b) Shen
(c) An
(d) Shapiro
(e) Purucker
(f) Li
-60 -55 -50 -45 -40 -35 -30 -25 -20 -15 -10 -5 0
Heat Conduction(mW m-2)

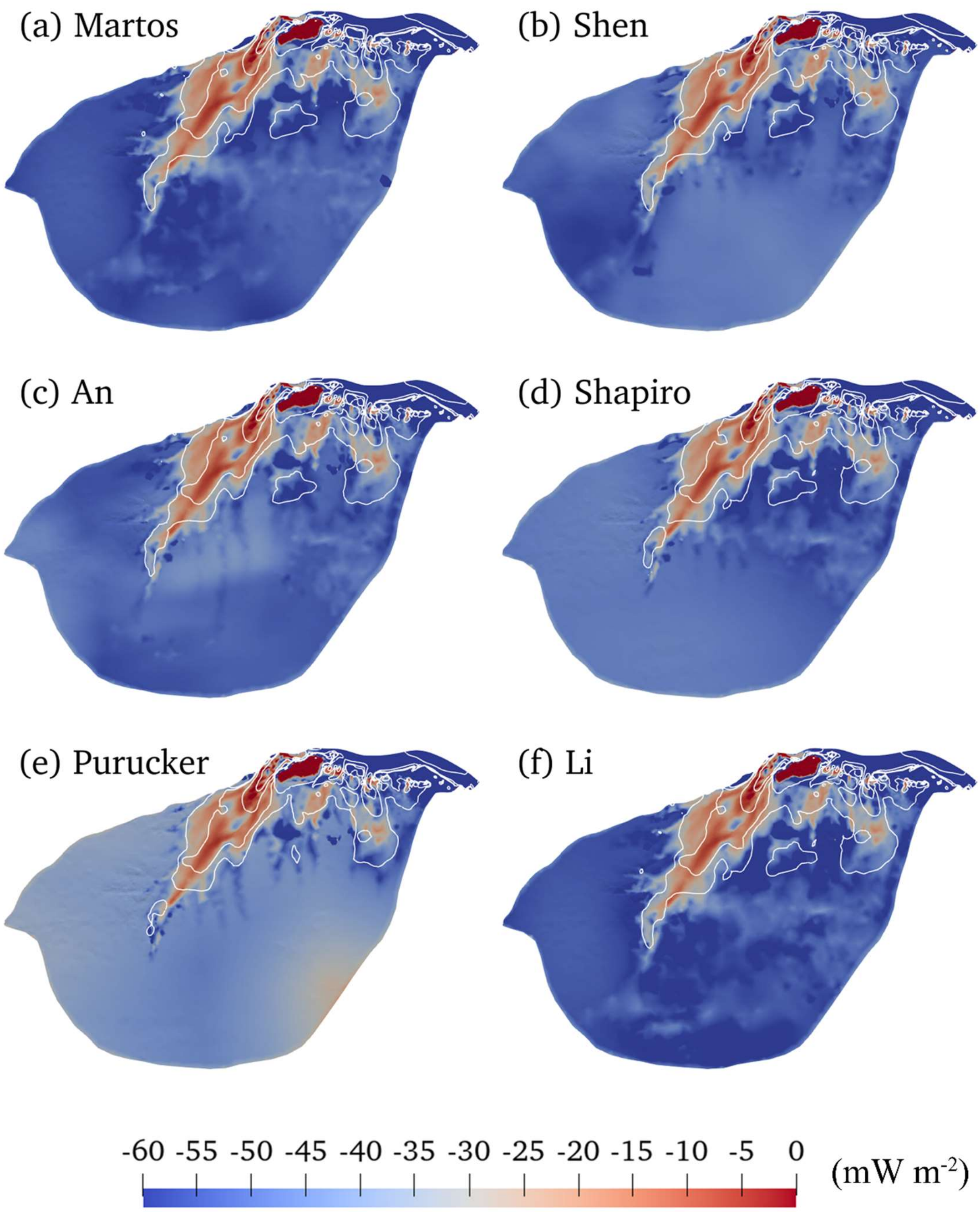

Fig. ~~6.~~8. Modelled heat change of basal ice by upward englacial heat conduction (unit: mW m^{-2}). The negative sign means that the upward englacial heat conduction causes heat loss from the basal ice as defined by the color bar with cooler colors representing more intense heat loss by conduction. (a) to (f) corresponding to the GHF (a) to (f) in Fig. ~~2~~2. The white solid curves represent modelled speed contours of 30, 50, 100 and 200 m yr^{-1}, the same as in Fig. 6b.

Fig. ~~6~~8 show the modelled heat change of basal ice by upward englacial heat conduction in the six experiments. In most regions of the fast-flowing tributaries ~~(Fig. 4a),~~with velocity higher than 30 m yr^{-1}, the heat loss caused by upward basal heat conduction is lower than ~~0~~-30 mW m^{-2} in all experiments~~.~~, reflecting the development of a temperate basal layer that limits the basal thermal gradient. For the vast inland areas, ~~most~~ experiments yield ~~high~~heat loss by upward heat conduction in the range of 45-60 mW m^{-2} except for the ~~Purucker~~ experiment driven by the Purucker (2013) GHF which has lower values around 30-45 mW m^{-2}. This is because the upward heat conduction equals GHF where basal temperature is below the pressure melting point, and the Purucker (2013) GHF is lower than the others.

4.3~~.3~~ Basal Friction Heat

~~Fig. 7 shows the~~There is no significant difference in modelled basal friction ~~heating maps in six~~heat across these 6 experiments~~.~~, reflecting the fact that all of them have been tuned to match the surface velocity observations. So, we show only the modelled basal friction driven by Martos et al. (2017) GHF (Fig. 5b). As expected, basal friction heat is high in fast-flowing regions. The three fast-flowing tributaries have friction ~~heating over~~heat amounting to more than 50 mW m^{-2} ~~and reach~~, with the Lambert and Kronshtadtskiy glaciers having 2000 mW m^{-2} at the grounding line.

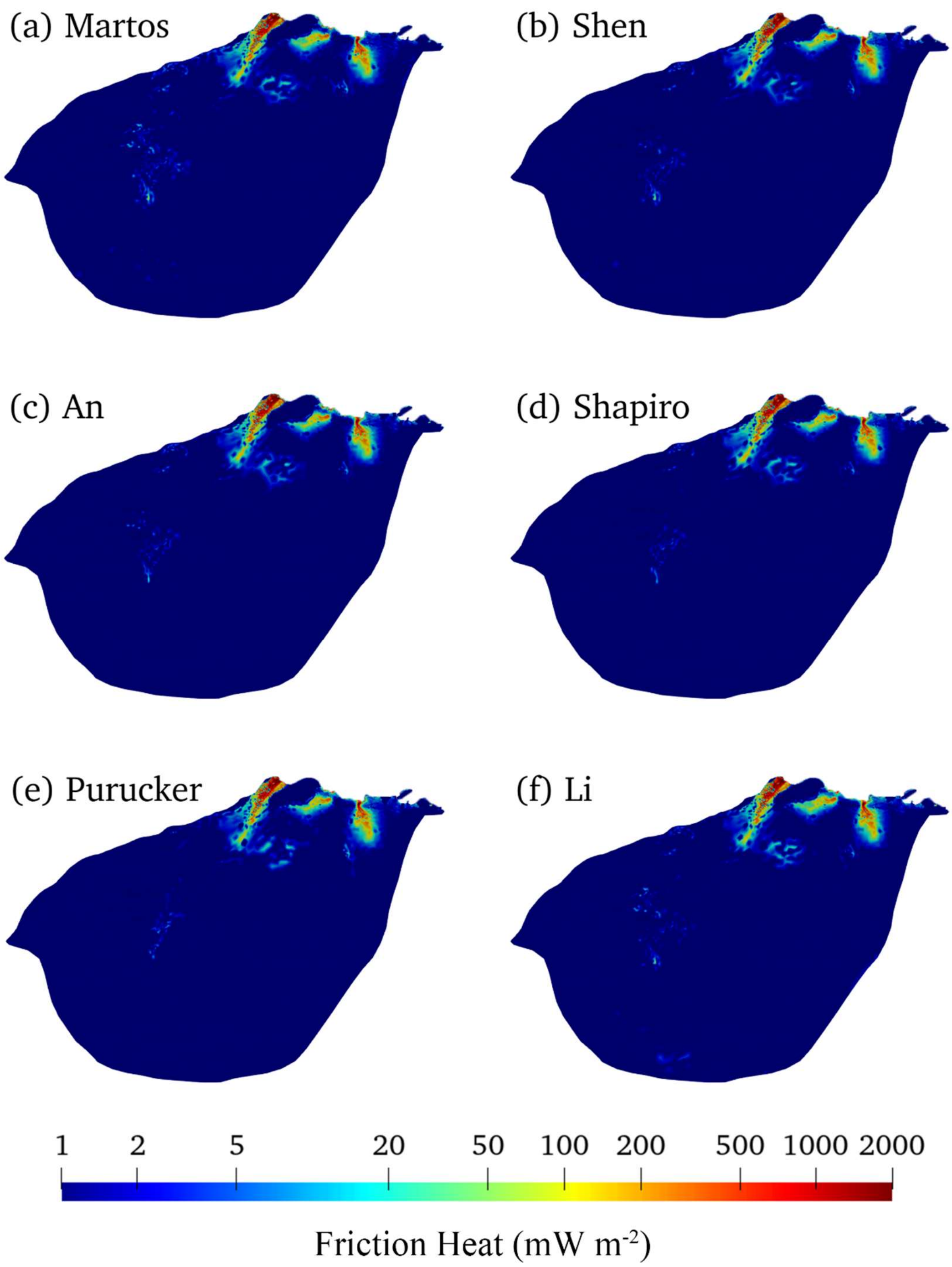

~~Fig. 7. Modeled basal friction heat (unit: mW m^{-2}), (a) to (f) corresponding to the GHF (a) to (f) in Fig. 2, respectively.~~

4.~~3.~~4 Basal Melt Rate

We get the basal melt rate using the thermal balance equation (Eq ~~19~~10). Fig. ~~8~~9 shows the modelled basal melt rate in the six experiments using different GHF. Regions with basal melt rate coincide with a warm base where basal temperatures reach the pressure-melting point. There are significant differences in the area ~~with~~of basal melting among the six experiments due to large variability in GHF. The experiments using Li et al. (2021) and Martos ~~experiments~~ et al. (2017) GHF yield the largest area with basal melting. In contrast, ~~Purucker~~the experiment using Purucker (2013) GHF gives the least area with basal melting (Fig. ~~8~~10).

The modelled basal melt rate is below 5 mm yr^{-1} in the parts of the vast inland region that are warm based. Higher basal melt ~~rate occurs~~rates occur in fast-flowing regions (Fig. ~~8Fig. 8)~~9) where frictional heat is high (Fig. ~~7~~5b), despite the differences in GHF (Fig. ~~4). Maximal basal melting~~2). Basal melt rate is above 10 mm yr^{-1} near the grounding line, reaching 500 mm yr^{-1} at the grounding line of the central flowline running onto Amery ice shelf. Thus, in fast-flowing regions, frictional heat is the dominant factor rather than GHF, consistent with Larour et al~~.,~~. (2012) who noted that slower flowing ice in the interior of the ice sheet will be more sensitive to the GHF, but frictional heat dominates GHF in regions of fast ice flow.

We use the positions of observed subglacial lakes to validate simulated regions with basal melting (Fig. ~~8~~9). The ~~Li experiment gives the best fit between the observed subglacial lakes and the~~ modelled warm base ~~region (Fig. 8f). The modelled warm base~~in the experiment using Li et al. (2021) GHF covers all the observed subglacial lakes in the domain~~,~~ (Fig. 9f), including the recently discovered second-largest subglacial lake in Antarctica (Cui et al., 2020b). The ~~Martos~~ warm base in the experiment ~~gives the next best fit~~ using Martos et al. (2017) GHF covers the second most observed subglacial lakes (Fig. ~~8a~~9a), and the ~~An~~ experiment using An et al. (2015) GHF the third (Fig. ~~8e~~9c). The ~~Shen~~ experiment using Shen et al. (2020) GHF captures two subglacial lakes in the southwest of the domain (Fig. ~~8b~~9b), while the ~~Shapiro~~ experiment using Shapiro and Ritzwoller (2004) GHF missed many known subglacial lakes in the southwest of the domain, but successfully captures the recently discovered second-largest subglacial lake (Fig. ~~8b~~9b, d). The ~~Purucker~~ experiment using Purucker et al. (2013) GHF performs worst in recovering subglacial lake locations (Fig. ~~8e~~9e).

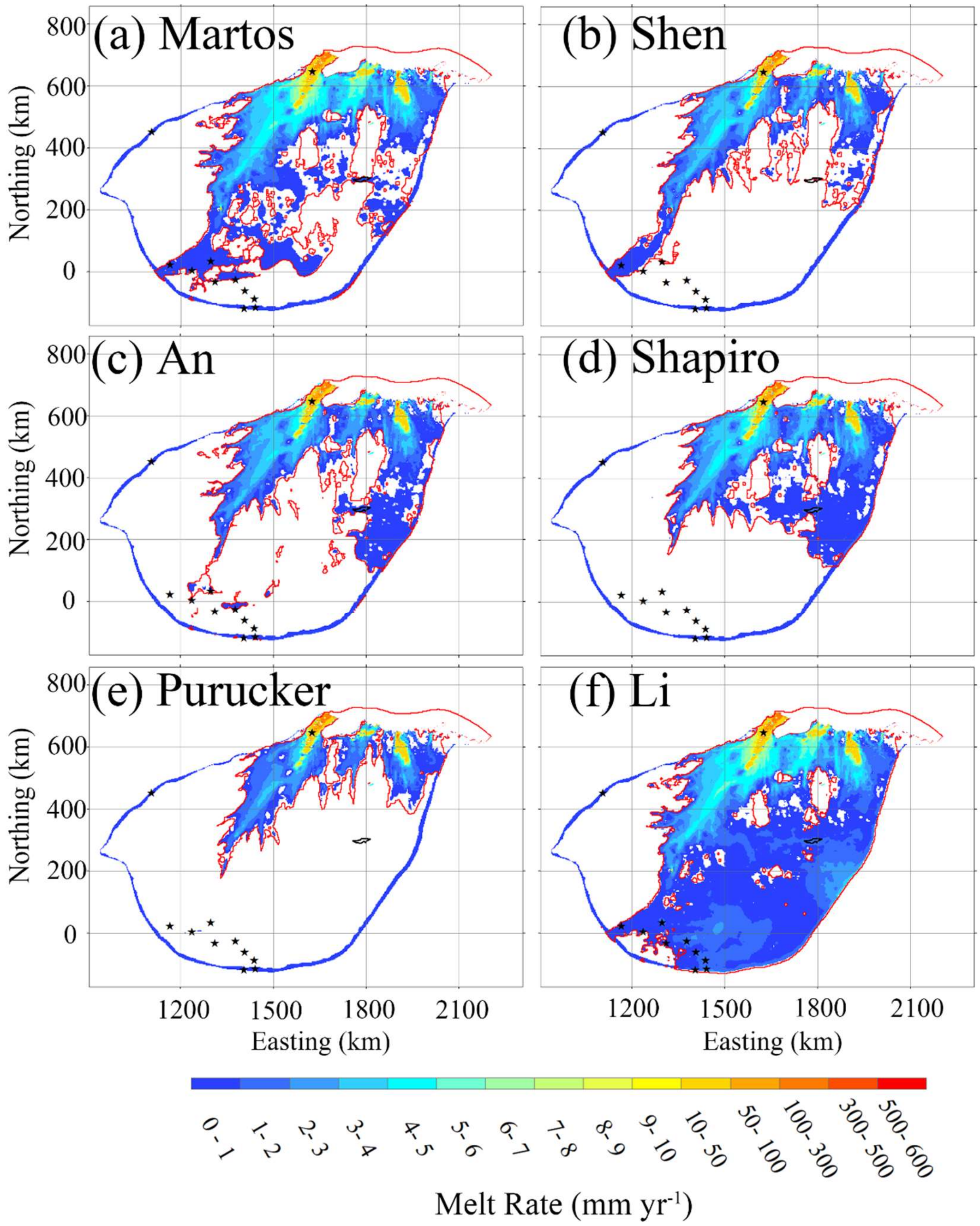

~~Fig. 8.~~

There are localized negative values of basal melt rate, indicating basal refreezing at three locations (Fig. 9). The modelled refreezing locations are generally characterized by large gradients in ice thickness, typically thinning by 700 m across a distance of 2 km. Radar surveys have not yet been done to confirm these freeze-on locations.

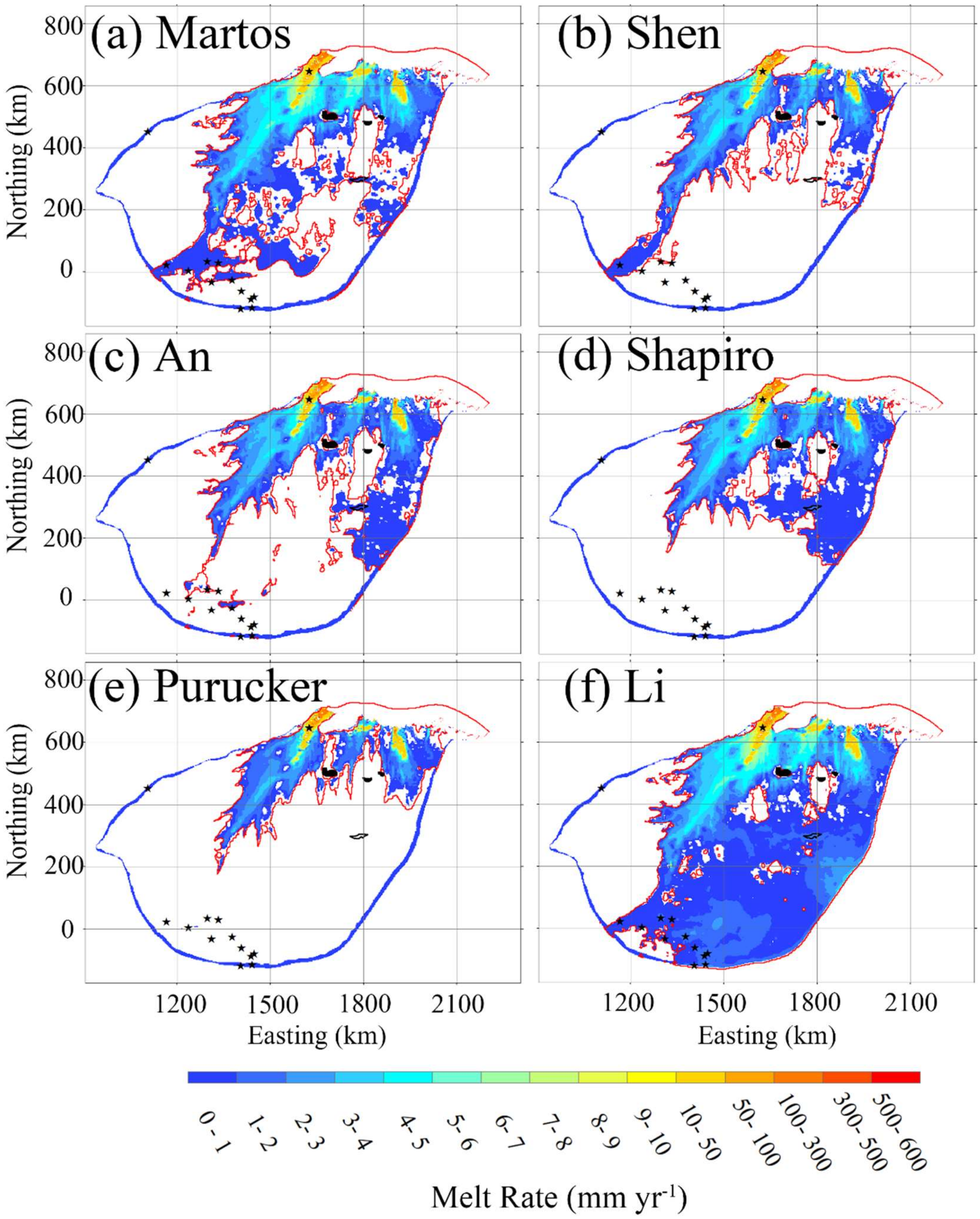

Fig. 9. Modelled basal melt rate (unit: mm yr^{-1}), (a) to (f) correspond to the GHF (a) to (f) in Fig. 2. The ice bottom at pressure-melting point is surrounded by a red contour. The stars denote the locations of observed subglacial lakes, and the area surrounded by the black line is the likely second largest subglacial lake in Antarctica. There is modelled basal refreezing at three local places painted in black.

5 Discussion

Uncertainties and bias in our simulations can come from several sources. We expect that the present-day accumulation rate field will be higher than the long-term average, because of lower accumulation rate during glacial periods. This will tend to increase the downward advection of cold ice in our model, lowering the basal temperature in comparison to reality. On the other hand, we also expect that the modern-day surface temperature will be higher than the long-term average temperature, again because of lower temperatures during glacial periods. This will tend to increase our modeled basal temperature in comparison with reality. It is unclear which of these competing biases is stronger.

Subglacial topography has an influence on geothermal heat at kilometer scales. Typically, it has been assumed that subglacial ridges receive less heat flow and subglacial valleys receive more heat flow, in comparison to the regional average (e.g., van der Veen et al., 2007; Colgan et al., 2021). However, the effect depends on subglacial rock type. Heat tends to follow the path of least resistance to the surface. The thermal conductivity of rock varies with lithology, and can be either greater or smaller than the thermal conductivity of ice (Willcocks & Hasterok, 2019), thus the sign of the topographic effect on GHF can be either negative or positive. Without knowing a priori whether the topographic effect will be positive or negative, it is hard to apply a topographic correction field to the GHF input field.

GHF distribution largely governs basal thermal conditions. Many previous studies (Larour et al., 2012; Pattyn, 2010; Pittard et al.,2016; Van Liefferinge and Pattyn, 2013; Van Liefferinge et al. 2018) on basal temperature and basal melt have used the Shapiro~~,~~ and Ritzwoller (2004), Fox~~,~~ Maule et al. (2005), Purucker~~,~~ (2013), and An et al. (2015) GHF datasets, with few making use of the more recent Martos et al. (2017) and Li ~~fields.~~et al. (2021) GHF datasets. In this study, we find that the Li et al. (2021) and Martos ~~experiments~~et al. (2017) GHF datasets have higher GHF than the earlier datasets in the Lambert-Amery domain and consequently have the largest area with warm base. The warmer basal conditions best match the observed distribution of subglacial lakes. However, it should be noted that observations of subglacial lakes are a one-sided constraint~~: a~~. A model result that misses the observed lakes is clearly too cold~~, but~~ at that location. But if the -model ~~puts warm-based conditions outside of the locations of the~~result shows basal melt at a place with no observed lakes, it is not clear whether this is because the model is too warm, or if the subglacial water exists in a form other than ponded lakes.

~~Our methodology builds on the earlier inversion method employed by Wolovick et al. (2021). Specifically, we~~A lake complex beneath Devon Island ice cap in Canada exists at temperatures well below pressure melting point due to large concentrations of dissolved salts (Rutishauser et al., 2018), and while no similar ones are known to exist beneath the Antarctic ice sheet, direct measurements of ice temperatures above water bodies are rare. Furthermore, relatively high electrical conductivity beds such as water saturated clays can give rise to false positives in radar detections of subglacial water bodies (Talalay et al., 2020).

Our simulations make improvements on previous approaches. We use the full-Stokes flow model in the inversion of basal friction field rather than a simplified physics model~~.~~ as in Wolovick et al. (2021a). We also improve on the treatment of the basal friction field by imposing ~~an increase in~~ a larger basal friction where the ice ~~bed~~bottom is colder than the pressure melting point, and which increases with temperature difference from freezing point. These modifications produce more physically meaningful results since we expect frozen beds to have high basal friction. Hence, the basal friction field is constrained by simulated temperatures in addition to producing the best fitting match of simulated and observed surface velocities.

Van Liefferinge and Pattyn (2013) estimated basal temperature for the Antarctica ice sheet using three GHF datasets (Fox~~, Sharpio,~~ Maule et al., 2005; Shapiro and Ritzwoller, 2004; Purucker, 2013), and each of the datasets were improved by the method in Pattyn (2010). Their modeled temperatures show spatial similarities to the ~~Purucker~~our experiment field ~~in our study~~using Purucker et al. (2013) GHF. Pittard et al. (2016) did sensitivity experiments of the Lambert-Amery glacial system based on 3 GHF fields (Fox~~, An, Sharpio~~ Maule et al., 2005; An et al., 2015; Shapiro and Ritzwoller, 2004) using the ice dynamics model PISM, and found that modelled basal temperature reached the pressure melting point only under the fast-flowing ice, with maximum melting rates of 500 mm yr^{-1} at places very close to the grounding line of the central flowline onto the Amery ice shelf. ~~This is similar to our modelled maximum basal melt at similar locations in the six experiments. However, their modelled region of basal melt is mainly confined to the Lambert glacier tributary and well matches only that of the Purucker experiment in our study.~~We also model maximum basal melt at similar locations in the six GHF experiments. However, the Pittard et al. (2016) region of basal melt is mainly confined to the Lambert glacier tributary and matches only that of our experiment using Purucker (2013) GHF.

We analyze the contribution of GHF and frictional heat to basal melt. The basal friction is a significant heat sources only under fast-flowing ice. ~~The~~Most GHF ~~distribution~~distributions (except Martos et al., 2017 and Li et al., 2021) in the grounded ice sheet ~~connected to~~near the ice shelf ~~is much more~~are homogeneous, but frictional heating ~~means that the melt rate~~ in the fast-flowing ice is more than 10 times higher than that in the slow-flowing ice. Thus slower flowing ice in the interior of the ice sheet is more sensitive to the GHF~~,~~ than fast-flowing ice (Larour et al., 2012).

GHF has its largest impact on the basal melt of the ~~vast~~ inland ice sheet. There are two principle ways to constrain GHF: (1) direct measurement (2) inversion by multiple geophysical methods. The GHFs used in this study are based on inversion of satellite or aero magnetic data and seismic tomography. Direct observations of heat flux are difficult to obtain in Antarctica, and satellite data are low resolution. The most efficient methods is to invert the heat flux through aerial geomagnetic observation such as for the Martos and Li GHF fields. However, there are still large data gaps in remote regions, especially in PEL, leaving just inversion using satellite magnetic data with a lower resolution. The Li et al. (2021)~~,~~ field uses the latest aeromagnetic data to estimate the GHF in the PEL region and this gives higher values than derived previously.

To validate the modelled basal melt, we use the locations of detected subglacial lakes. There may be many other undiscovered subglacial lakes beneath the study area, and further discoveries would help us validate the model results, and possibly refine GHF maps. In addition, further observational constraints with a two-sided sensitivity to ice temperature, such as observations of subglacial freeze-on or measurements of englacial attenuation, would help us to identify areas in which the GHF maps are too warm, in addition to those areas in which they are too cold.

6 Conclusions

In this paper, we estimate the basal thermal conditions of the Lambert-Amery system by coupling a forward model and an inverse model, based on six different GHF datasets. We analyze the contribution of GHF, heat ~~condition~~conduction, and basal friction to the modelled basal melt rate. We verify the result using the locations of all known subglacial lakes, and evaluate the reliability of six GHF datasets in our study domain.

Our approach is distinct from that used to find GHF fields employed by Wolovick et al. (2021a), in particular the use of a full Stokes model allows the method to be extended to fast flowing ice streams and ice shelf domains where neither the shallow ice nor shallow shelf-approximations are valid. We also improve the basal friction calculation to include information on the basal ice temperature relative to its pressure melting point. This procedure results in removal of unrealistic noise manifested as local spikes in modelled basal friction heat.

We find significant differences in ~~area with basal melting~~ the spatial extent of temperate ice in the slow flowing areas among the six experiments due to large variability in GHF. The experiments using Li et al. (2021) and the Martos ~~fields~~ et al. (2017) GHF yield the largest area with basal melting, and match ~~best with~~ the subglacial lake locations best. In contrast, the experiments using Purucker ~~field~~(2013) GHF gives the least area with basal melting and the worst match with subglacial lakes locations. We suggest GHF datasets from Li et al. (2021) and Martos et al. (2017) as the most suitable choice for this study region. We cannot make our own GHF map from our analysis since while we can pick the GHF in places where the Li and Martos geothermal heat flow maps are consistent and both agree with the observations, we do not know which (if either) are correct where the Li and Martos GHF datasets disagree and there are no observations. In order to make this determination we would need additional observational constraints on the basal thermal state, such as measured basal temperatures from deep ice cores, or observed refreeze-on, but neither are available in the region.

~~The modelled high basal friction heating regions are consistent with the fast flowing regions.~~ The fast flowing region has smaller modelled basal friction coefficients, and faster basal velocities~~.~~, but there are large differences in basal melting rates between the 6 GHF datasets. The fast-flowing tributaries have frictional heating in the range of 50-2000 mW m^{-2}. In the vast inland areas, our experiments generally yield high upward heat conduction in the range of 45-60 mW m^{-2} which means that GHF dominates the heat content of the basal ice in the slow flow regions. The modelled basal melt rate reaches 50-500 mm yr^{-1} locally in three very fast flow tributaries (Lambert, Lepekhin and Kronshtadtskiy glaciers~~), to~~) feeding the Amery ice shelf, and is in the range of 0-5 mm yr^{-1} in the inland region.

Data availability

All data sets used are publicly available.

Acknowledgments

This work was supported by the National Natural Science Foundation of China (No. 41941006) and National Key Research and Development Program of China (~~2018YFC1406104~~2021YFB3900105).

References

An, M., Wiens, D. A., Zhao, Y., Feng, M., Nyblade, A. A., Kanao, M., et al.: Temperature, lithosphere-asthenosphere boundary, and heat flux beneath the Antarctic Plate inferred from seismic velocities, J. Geophys. Res.: Solid Earth, 120, 359-383, https://doi.org/10.1002/2014jb011332, 2015.

Arthern, R. J., Winebrenner, D. P., & Vaughan, D. G. Antarctic snow accumulation mapped using polarization of 4.3-cm wavelength microwave emission. Journal of Geophysical Research: Atmospheres, 111(D6), 2006, D06107. https://doi.org/10.1029/2004JD005667

Budd, W. F., Warner, R. C., Jacka, T., Li, J., and Treverrow, A.: Ice flow relations for stress and strain-rate components from combined shear and compression laboratory experiments, J. Glaciol., 59, 374-392, https://doi.org/10.3189/2013JoG12J106, 2013.

Colgan, W., MacGregor, J. A., Mankoff, K. D., Haagenson, R., Rajaram, H., Martos, Y. M., et al. (2021). Topographic correction of geothermal heat flux in Greenland and Antarctica. Journal of Geophysical Research: Earth Surface, 126, e2020JF005598. https://doi. org/10.1029/2020JF005598

Cuffey, K. M., and Paterson, W. S. B.: The physics of glaciers, fourth edition, Elsevier, Burlington, 2010.

Cui, X., Jeofry, H., Greenbaum, J. S., Guo, J., Li, L., Lindzey, L. E., et al.: Bed topography of Princess Elizabeth Land in East Antarctica, Earth Syst. Sci. Data, 12, 2765-2774, https://doi.org/10.5194/essd-2020-126, 2020a.

Cui, X., Lang, S., Guo, J., and Sun, B.: Detecting and Searching for subglacial lakes through airborne radio-echo sounding in Princess Elizabeth Land (PEL), Antarctica, E3S Web of Conferences, 163, https://doi.org/10.1051/e3sconf/202016304002, 2020b.

Dziadek, R., Ferraccioli, F., and Gohl, K.: High geothermal heat flow beneath Thwaites Glacier in West Antarctica inferred from aeromagnetic data, Commun. Earth Environ., 2, https://doi.org/ARTN 16210.1038/s43247-021-00242-3, 2021.

Fox Maule, C., Purucker, M. E., Olsen, N., & Mosegaard, K. (2005). Heat flux anomalies in Antarctica revealed by satellite magnetic data. Science, 309(5733), 464 – 467. https://doi.org/10.1126/science.1106888

Fretwell, P., Pritchard, H. D., Vaughan, D. G., Bamber, J. L., Barrand, N. E., Bell, R., et al.: Bedmap2: improved ice bed, surface and thickness datasets for Antarctica, The Cryosphere, 7, 375–393, https://doi.org/10.5194/tc-7-375-2013, 2013

Fricker, H. A., Siegfried, M. R., Carter, S. P., and Scambos, T. A.: A decade of progress in observing and modelling Antarctic subglacial water systems, Philosophical Transactions of the Royal Society A: Mathematical, Physical and Engineering Sciences, 374, 20140294, https://doi.org/10.1098/rsta.2014.0294, 2016.

Gagliardini, O., Zwinger, T., Gillet-Chaulet, F., Durand, G., Favier, L., Fleurian, B. d., et al.: Capabilities and performance of Elmer/Ice, a new-generation ice sheet model, Geosci. Model Dev., 6, 1299-1318, https://doi.org/10.5194/gmd-6-1299-2013, 2013.

Geuzaine, C., and Remacle, J. F.: Gmsh: A 3-D finite element mesh generator with built-in pre- and post-processing facilities, Int. J. Numer. Meth. Eng., 79, 1309-1331, https://doi.org/10.1002/nme.2579, 2009.

Greve R, Blatter H, Dynamics of Ice Sheets and Glaciers, Springer, 2009.

Gillet-Chaulet, F., Gagliardini, O., Seddik, H., Nodet, M., Durand, G., Ritz, C., et al.: Greenland ice sheet contribution to sea-level rise from a new-generation ice-sheet model, The Cryosphere, 6, 1561-1576, https://doi.org/10.5194/tc-6-1561-2012, 2012.

Hansen, P., and Johnston, P.: Computational inverse problems in electrocardiology, 2000.

King, M. A., Coleman, R., Morgan, P. J., and Hurd, R. S.: Velocity change of the Amery Ice Shelf, East Antarctica, during the period 1968–1999, J. Geophys. Res.-Earth, 112. doi:10.1130/g37220.1, 2007.

Larour, E., Morlighem, M., Seroussi, H., Schiermeier, J., and Rignot, E.: Ice flow sensitivity to geothermal heat flux of Pine Island Glacier, Antarctica, J. Geophys. Res.-Earth, 117, https://doi.org/10.1029/2012jf002371, 2012.

Le Brocq, A. M., Payne, A. J., and Vieli, A.: An improved Antarctic dataset for high resolution numerical ice sheet models (ALBMAP v1), Earth Syst. Sci. Data, 2, 247-260, https://doi.org/10.5194/essd-2-247-2010, 2010.

Li, L., Tang, X., Guo, J., Cui, X., Xiao, E., Latif, K., et al.: Inversion of Geothermal Heat Flux under the Ice Sheet of Princess Elizabeth Land, East Antarctica, Remote Sensing, 13. doi:10.3390/rs13142760, 2021.

Martos, Y. M., Catalán, M., Jordan, T. A., Golynsky, A., Golynsky, D., Eagles, G., et al.: Heat flux distribution of Antarctica unveiled, Geophys. Res. Lett., 44, 11,417-411,426, https://doi.org/10.1002/2017gl075609, 2017.

Maule, C. F., Purucker, M. E., Olsen, N., and Mosegaard, K.: Heat flux anomalies in Antarctica revealed by satellite magnetic data, Science, 309, 464-467, https://doi.org/10.1126/science.1106888, 2005.

Morlighem, M., Rignot, E., Binder, T., Blankenship, D., Drews, R., Eagles, G., et al.: Deep glacial troughs and stabilizing ridges unveiled beneath the margins of the Antarctic ice sheet, Nat. Geosci., 13, 132-137, https://doi.org/10.1038/s41561-019-0510-8, 2020.

Morlighem, M., Rignot, E., Seroussi, H., Larour, E., Ben Dhia, H., and Aubry, D.: Spatial patterns of basal drag inferred using control methods from a full-Stokes and simpler models for Pine Island Glacier, West Antarctica, Geophys. Res. Lett., 37, https://doi.org/10.1029/2010gl043853, 2010.

Mouginot, J., Scheuchl, B., and Rignot, E.: MEaSUREs Antarctic Boundaries for IPY 2007-2009 from Satellite Radar, Version 2, National Snow and Ice Data Center, 10, https://doi.org/doi.org/10.5067/AXE4121732AD, 2017.

Näslund, J.-O., Jansson, P., Fastook, J. L., Johnson, J., and Andersson, L.: Detailed spatially distributed geothermal heat-flow data for modeling of basal temperatures and meltwater production beneath the Fennoscandian ice sheet, Ann. Glaciol., 40, 95-101, https://doi.org/10.3189/172756405781813582, 2005.

Pattyn, F.: Antarctic subglacial conditions inferred from a hybrid ice sheet/ice stream model, Earth Planet. Sc. Lett., 295, 451-461, https://doi.org/10.1016/j.epsl.2010.04.025, 2010.

Pittard, M., Roberts, J., Galton-Fenzi, B., and Watson, C.: Sensitivity of the Lambert-Amery glacial system to geothermal heat flux, Ann. Glaciol., 57, 56-68, https://doi.org/10.1017/aog.2016.26, 2016.

Rutishauser A., Blankenship, D. D., Sharp, M., Skidmore, M. L., Greenbaum, J. S., Grima, C., Schroeder, D. M., Dowdeswell, J. A., Young, D. A., Discovery of a hypersaline subglacial lake complex beneath Devon Ice Cap, Canadian Arctic, Sci. Adv.2018; 4: eaar4353

Purucker, M. E.: Geothermal heat flux data set based on low resolution observations collected by the CHAMP satellite between 2000 and 2010, and produced from the MF-6 model following the technique described in Fox Maule et al. (2005), 2012. Retrieved from http://websrv.cs.umt.edu/isis/index.php/Antarctica_Basal_Heat_Flux

Rezvanbehbahani, S., Stearns, L. A., Van der Veen, C. J., Oswald, G. K. A., and Greve, R.: Constraining the geothermal heat flux in Greenland at regions of radar-detected basal water, J. Glaciol., 65, 1023-1034, https://doi.org/10.1017/jog.2019.79, 2019.

Rignot, E., Mouginot, J., and Scheuchl, B.: MEaSUREs InSAR-based Antarctica ice velocity map, version 2, Boulder, Colorado USA. NASA National Snow and Ice Data Center Distributed Active Archive Center, https://doi.org/doi.org/10.5067/D7GK8F5J8M8R, 2017.

Rignot, E., Mouginot, J., Scheuchl, B., Van Den Broeke, M., Van Wessem, M. J., and Morlighem, M.: Four decades of Antarctic Ice Sheet mass balance from 1979-2017, P. Natl. Acad. Sci. USA, 116, 1095-1103, https://doi.org/10.1073/pnas.1812883116, 2019.

Shapiro, N. M., and Ritzwoller, M. H.: Inferring surface heat flux distributions guided by a global seismic model: particular application to Antarctica, Earth Planet. Sc. Lett., 223, 213-224, https://doi.org/10.1016/j.epsl.2004.04.011, 2004.

Shen, W., Wiens, D. A., Lloyd, A. J., and Nyblade, A. A.: A geothermal heat flux map of Antarctica empirically constrained by seismic structure, Geophys. Res. Lett., 47, https://doi.org/10.1029/2020gl086955, 2020.

Talalay, P., Li, Y., Augustin, L., Clow, G. D., Hong, J., Lefebvre, E., Markov, A., Motoyama, H. and Ritz, C., Geothermal heat flux from measured temperature profiles in deep ice boreholes in Antarctica, The Cryosphere, 14, 4021-4037, 2020

van der Veen, C. J., Leftwich, T., von Frese, R., Csatho, B. M., & Li, J. Subglacial topography and geothermal heat flux: Potential interactions with drainage of the

Greenland ice sheet. Geophysical Research Letters, 34(12), 2007.

Van de Berg, W. J., Van den Broeke, M. R., Reijmer, C. H., & Van Meijgaard, E. Characteristics of the Antarctic surface mass balance, 1958-2002, using a regional atmospheric climate model. Annals of Glaciology, 41(1), 97-104, 2005. https://doi.org/10.3189/172756405781813302

Van Liefferinge, B., and Pattyn, F.: Using ice-flow models to evaluate potential sites of million year-old ice in Antarctica, Clim. Past, 9, 2335-2345, https://doi.org/10.5194/cp-9-2335-2013, 2013.

Van Liefferinge, B., Pattyn, F., Cavitte M. G. P., et al.: Promising Oldest Ice sites in East Antarctica based on thermodynamical modelling. The Cryosphere, 12, 2773-87, https://doi.org/10.5194/tc-12-2773-2018, 2018.

Willcocks, S., & Hasterok, D. Thermal refraction: Impactions for subglacial heat flux. ASEG Extended Abstracts, 2019(1), 1–4. Taylor & Francis. https://doi.org/10.1080/22020586.2019.12072986

Wolovick, M. J., Moore, J. C., and Zhao, L~~:~~. Joint inversion for surface accumulation rate and geothermal heat flow from ice-penetrating radar observations at Dome A, East Antarctica. Part I: model description, data constraints, and inversion results, J. Geophys. Res.-Earth, 126, 2021. https://doi.org/10.1029/2020jf005937, ~~2021~~2021a.

Wolovick, M. J., Moore, J. C., and Zhao, L. Joint inversion for surface accumulation rate and geothermal heat flow from ice-penetrating radar observations at Dome A, East Antarctica. Part II: Ice sheet state and geophysical analysis. Journal of Geophysical Research: Earth Surface, 126, e2020JF005936, 2021b. https://doi.org/10.1029/2020JF005936

Wright, A., and Siegert, M.: A fourth inventory of Antarctic subglacial lakes, Antarct. Sci., 24, 659-664, https://doi.org/10.1017/s095410201200048x, 2012.

Zhao, C., Gladstone, R. M., Warner, R. C., King, M. A., Zwinger, T., and Morlighem, M.: Basal friction of Fleming Glacier, Antarctica – Part 1: Sensitivity of inversion to temperature and bedrock uncertainty, The Cryosphere, 12, 2637-2652, https://doi.org/10.5194/tc-12-2637-2018, 2018.